Journal of Marine Research, 57, 847–884, 1999

Lattice Boltzmann solutions of the three-dimensional planetary geostrophic equations

by Rick Salmon[1]

ABSTRACT

We use the lattice Boltzmann method as the basis for a three-dimensional, numerical ocean circulation model in a rectangular basin. The fundamental dynamical variables are the populations of mass- and buoyancy-particles with prescribed discrete velocities. The particles obey collision rules that correspond, on the macroscopic scale, to planetary geostrophic dynamics. The advantages of the model are simplicity, stability, and massively parallel construction. By the special nature of its construction, the lattice Boltzmann model resolves upwelling boundary layers and unsteady convection. Solutions of the model show many of the features predicted by ocean circulation theories.

1. Introduction

This is the second in a series of papers in which it is hoped to develop simple, efficient, numerical ocean circulation models based upon the lattice Boltzmann (LB) method, a method of computational fluid dynamics in which the fundamental dependent variables are the populations of particles with prescribed discrete velocities. The particles obey simple collision rules that determine the macroscopic fluid dynamics. The advantages of the LB method are simplicity, stability, and massively parallel computer code; the primary disadvantage is a lack of flexibility in comparison to more conventional models based upon finite differences or finite elements. Although widely used for about 10 years, the LB method had not previously been applied to rotating fluids.

The earlier paper (Salmon, 1999, hereafter S99) applied the LB method to the rotating shallow water equations in the form of the "reduced gravity model" for a homogeneous, wind-driven layer of fluid overlying a deeper layer that remains everywhere at rest. Although the reduced gravity model is a respectable model of the wind-driven ocean circulation, S99 emphasized *method,* offering a nearly self-contained introduction to LB theory, the Chapman-Enskog expansion, and some connections to topics—balanced motion, fast and slow modes—of greater familiarity to geophysical fluid dynamicists.

In this paper, we apply the LB method to the three-dimensional planetary geostrophic equations (2.1), which omit inertia but include the advection of buoyancy. In this paper, the emphasis is somewhat more equally divided between the development of the LB algorithm

1. Scripps Institution of Oceanography, University of California, La Jolla, California 92093-0225, U.S.A. ***email: rsalmon@ucsd.edu***

in Sections 2–5, and the discussion of its solutions in Section 6. Although the present paper is self-contained, it does not repeat S99's pedagogical introduction to LB. Therefore, readers who are unfamiliar with the LB method may wish to read S99 before attempting Sections 2–4 below. On the other hand, readers with no interest in the method can proceed directly to Section 5.

In Sections 2–4 and in the appendices, we derive the lattice Boltzmann algorithm summarized in Section 5 and demonstrate its equivalence to the time-dependent equations (5.8) at the second order of the Chapman-Enskog expansion. Our derivation differs from more typical LB applications in several respects. First, because the vertical spacing between lattice points is so much smaller than the horizontal spacing, and because the particles must hop from lattice point to lattice point in a time step, the particles move vertically at a speed much smaller than their horizontal speed. Because of this disparity in particle speeds, the "vertical pressure" is much smaller than the "horizontal pressure," and recovery of the right dynamics requires compensating adjustments that amount to an enhancement of the friction coefficient in the vertical momentum equation. However, the effects of this enhancement seem to be wholly beneficial: Sidewall boundary layers are resolved, the time step may be larger than in conventional primitive equation models, and the most unstable convective motions have horizontal scales resolved by the model.

Second, buoyancy is incorporated by introducing buoyancy particles that make no direct contribution to the mass, rather than by the more usual method of introducing "hot" and "cold" massive particles. The buoyancy-particle method proves essential to attaining the high Prandtl number necessary when inertia is omitted from ocean dynamics.

Third, as in S99, Coriolis force is an essential part of the dynamics, and Section 4 presents a method for incorporating Coriolis force that is vastly superior to the clumsy and inefficient predictor-corrector method used in S99. In the method of Section 4, an impulse corresponding to the action of Coriolis force for an interval of one half time step is distributed among the particles before and after each streaming step. The resulting LB cycle is . . . *spin—collide—spin—stream—spin—collide* . . . , where *collide* and *stream* denote the usual collision and streaming steps, and *spin* denotes the Coriolis impulse step. The presence of two Coriolis steps per cycle proves vital to maintaining second-order accuracy in the Chapman-Enskog expansion.

In Section 5 we summarize the complete LB algorithm, a cycle of 6 simple operations. Then we analyze the corresponding dynamical equations (5.8). In steady state, (5.8) reduce to (2.1) except for the previously mentioned enhancement of the viscosity coefficients in the vertical momentum equation. This enhancement means that departures from hydrostatic balance could be as large as the departures from geostrophic balance, but solutions of the LB equations with no-stress boundary conditions prove to be hydrostatic, except in relatively small regions of strong convection.

In Section 6 we examine 3 solutions of the LB model with 50^3 resolution. The solutions are driven by a 2-gyre wind stress and diabatic forcing. In one of the solutions, the diabatic forcing is contrived to maintain static stability, and no convection occurs. In another

solution, the ocean is cooled at the surface, and unsteady convection occurs on horizontal lengthscales resolved by the model. In the third solution, we impose convective adjustment in regions of static instability. The convective adjustment increases static stability but also generates lattice-scale noise; fortunately, the convective adjustment seems dispensable. All 3 solutions contain numerous features predicted by ocean circulation theories and found in more conventional calculations.

2. The lattice Boltzmann method

We seek a lattice Boltzmann (LB) model for the planetary geostrophic equations in Cartesian coordinates. In steady state, the equations are:

$$\begin{aligned} \nabla_3 \cdot \mathbf{v} &= 0 \\ f\mathbf{k} \times \mathbf{u} &= -\nabla\phi + A_h\nabla^2\mathbf{u} + A_v\mathbf{u}_{zz} \\ 0 &= -\phi_z + \theta + A_h\nabla^2 w + A_v w_{zz} \\ \mathbf{v} \cdot \nabla_3\theta &= \kappa_h\nabla^2\theta + \kappa_v\theta_{zz}. \end{aligned} \tag{2.1}$$

Here, $\mathbf{x} = (x, y, z)$ is the coordinate in the (eastward, northward, upward) direction with corresponding unit vector $(\mathbf{i}, \mathbf{j}, \mathbf{k})$; $\mathbf{v} = (\mathbf{u}, w) = (u, v, w)$ is the velocity; f is the Coriolis parameter; ϕ is the pressure (divided by a constant representative density); and θ is the buoyancy. Our notation is $\nabla_3 \equiv (\partial_x, \partial_y, \partial_z)$ and $\nabla \equiv (\partial_x, \partial_y)$. Subscript z denotes ∂_z. (A_h, A_v) and (κ_h, κ_v) are the (horizontal, vertical) eddy coefficients for momentum and buoyancy, respectively. We temporarily omit the wind and diabatic forcing terms. The planetary geostrophic equations have become increasingly popular as the basis for numerical ocean circulation models; see, for example, Huck *et al.* (1999) and references therein.

Although we prefer to work with dimensional variables, for future use we record the standard nondimensional form of (2.1). Let L be the ocean basin width and H the depth. Let U be a representative horizontal velocity. Then, scaling x and y by L, z by H, u and v by U, w by $W \equiv \delta_b U$, where $\delta_b \equiv H/L$ is the aspect ratio based on the basin size, f by representative value f_0, ϕ by $f_0 UL$, and θ by $f_0 UL/H$; we obtain (2.1) in the nondimensional form,

$$\begin{aligned} \nabla_3 \cdot \mathbf{v} &= 0 \\ f\mathbf{k} \times \mathbf{u} &= -\nabla\phi + E_h\nabla^2\mathbf{u} + E_v\mathbf{u}_{zz} \\ 0 &= -\phi_z + \theta + \delta_b^2 E_h\nabla^2 w + \delta_b^2 E_v w_{zz} \\ \mathbf{v} \cdot \nabla_3\theta &= D_h\nabla^2\theta + D_v\theta_{zz} \end{aligned} \tag{2.2}$$

where

$$E_h = \frac{A_h}{f_0 L^2}, \qquad E_v = \frac{A_v}{f_0 H^2}, \qquad D_h = \frac{\kappa_h}{UL}, \qquad D_v = \frac{\kappa_v}{WH}, \tag{2.3}$$

and δ_b are small parameters.

In the lattice Boltzmann method, we replace the fluid by a system of discrete particles that move from lattice point to adjacent lattice point in a time step Δt. Inhomogeneous fluid requires 2 types of particle: *mass particles,* which carry mass and momentum, and *buoyancy particles,* which only carry buoyancy. At every time step, all the particles present at each lattice point "collide." The strategy is to prescribe collision rules that make the particle dynamics approximate (2.1) as closely as possible. For reviews of the lattice Boltzmann method, see Benzi *et al.* (1992), Rothman and Zaleski (1997) and Chen and Doolen (1998).

To simplify the presentation, we temporarily assume that the buoyancy is uniform ($\theta \equiv 0$). Then no buoyancy particles are required. We also neglect both Coriolis and external forces. In the following section, we introduce buoyancy and discuss the buoyancy particles. In Section 4, we incorporate forcing.

We take the lattice to be a regular Cartesian grid with a horizontal spacing of Δx and a vertical spacing of Δz between lattice points. Refer to Figure 1. At each lattice point, the mass particles move in one of 14 directions at a speed just sufficient to reach the next lattice point in a time step. Thus the 2 particles moving parallel to the z-axis move at uniform speed $c_v \equiv \Delta z/\Delta t$, while the 4 particles moving parallel to the x- or y-axis move at speed $c_h \equiv \Delta x/\Delta t$. The complete set of particle velocities is given by

$$\mathbf{c}_{nmk} = (nc_h, mc_h, kc_v), \tag{2.4}$$

where $\{(n, m, k)\}$ is the 15-member set of integer triplets whose elements correspond to: the rest particle ($n = m = k = 0$); the 6 particles moving parallel to one of the 3 coordinate axes (for which 2 of (n, m, k) vanish, and the third is ± 1); and the 8 particles moving along the diagonals within each octant (for which all 3 of (n, m, k) are ± 1). This 15-member set represents the smallest set of particle velocities with sufficient symmetry to approximate (2.1) in the appropriate limit. Although the rest particle does not move, it interacts with the other particles through collisions. In homogeneous fluid the rest particle is dispensable, but our method of incorporating the buoyancy force will require the rest particle to be present.

Let $\rho_{nmk}(\mathbf{x}, t)$ be the contribution of the mass particle moving with velocity (2.4) at lattice point $\mathbf{x}$ and time t to the "density"

$$\rho(\mathbf{x}, t) \equiv \sum_{nmk} \rho_{nmk}(\mathbf{x}, t), \tag{2.5}$$

a dimensionless quantity whose precise physical meaning becomes clear as the development proceeds. Thus, for example, $\rho_{100}(\mathbf{x}, t)$ is the density of the particle moving in the direction of the positive x-axis. The summation in (2.5) is over the 15-member set just described. We also define the fluid velocity,

$$\mathbf{v}(\mathbf{x}, t) \equiv \sum_{nmk} \mathbf{c}_{nmk}\rho_{nmk}(\mathbf{x}, t), \tag{2.6}$$

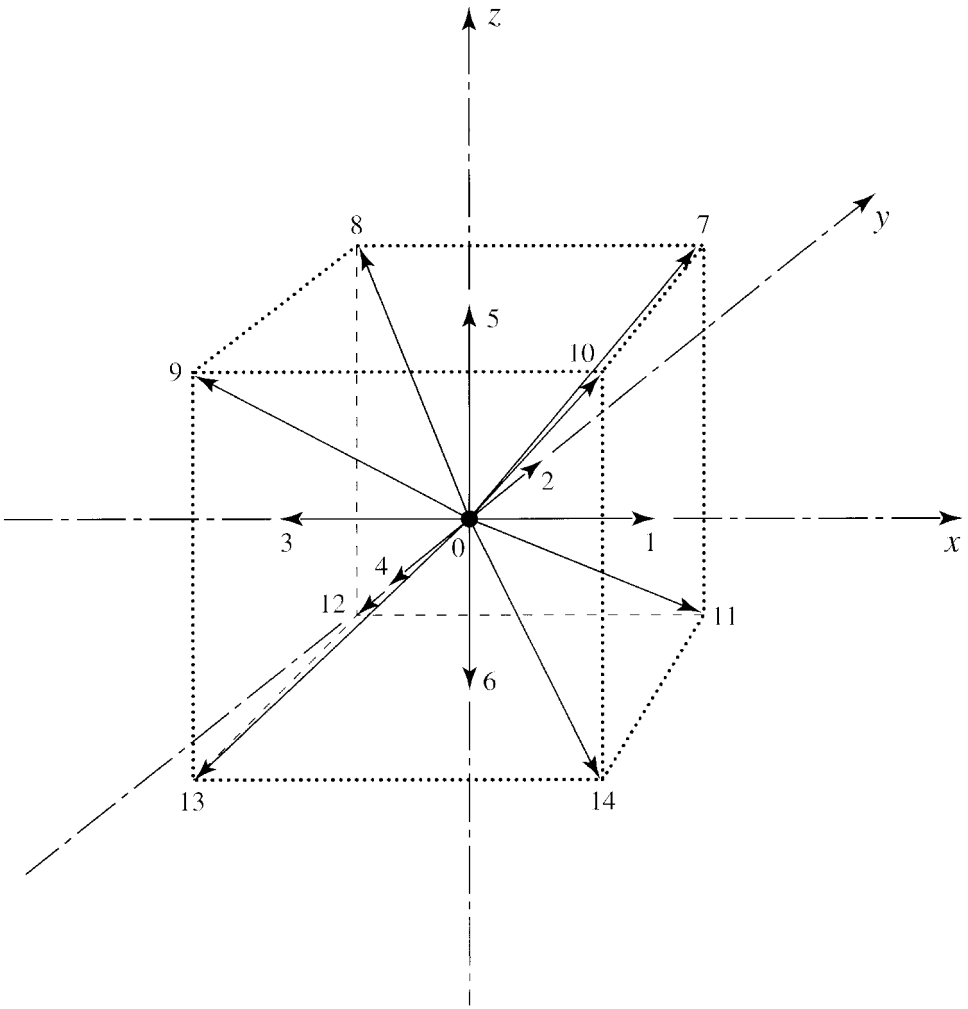

Figure 1. At every time step, each mass particle (except the rest particle denoted 0) moves in one of 14 directions to a neighboring lattice point. The particles numbered 1 to 6 move parallel to one of the coordinate axes. The mass particles numbered 7 to 14 move in diagonal directions not parallel to any coordinate axis or plane. The 6 buoyancy particles move only in the directions parallel to a coordinate axis. There is no rest particle for buoyancy.

where $\mathbf{c}_{nmk}$ is given by (2.4).[2] Although the particles move at fixed speeds, the fluid velocity (2.6) varies continuously. The defining equations (2.5–6) relate the 15 "microscopic" dependent variables $\{\rho_{nmk}(\mathbf{x}, t)\}$ to the 4 "macroscopic" dependent variables $\{\rho(\mathbf{x}, t), \mathbf{v}(\mathbf{x}, t)\}$ of the continuum. (But note that $\rho(\mathbf{x}, t)$ does not actually appear in (2.1).)

2. In usual applications of the LB method, the analogue of (2.6) contains a factor ρ on its left-hand side. Our definition is motivated by a desire that $\mathbf{v}$ rather than $\rho\mathbf{v}$ be exactly nondivergent when the fluid motion is steady.

In the absence of forcing, LB dynamics comprises 2 steps: a collision step, in which all the particles at the same lattice point interact, followed by a streaming step, in which particles move in the appropriate direction to the next lattice point. The interaction takes the form of a relaxation toward the local equilibrium state $\{\rho^{eq}_{nmk}(\mathbf{x}, t)\}$, where the ρ^{eq}_{nmk} are prescribed functions of ρ and $\mathbf{v}$ at the same lattice point. Thus the collision step takes the form

$$\rho'_{nmk} = \rho_{nmk} - \lambda\Delta t(\rho_{nmk} - \rho^{eq}_{nmk}), \tag{2.7}$$

where λ is the constant relaxation coefficient, and the prime denotes the value immediately after the collision. In (2.7), all the variables are evaluated at the same lattice point and time. The streaming step takes the form

$$\rho_{nmk}(\mathbf{x} + \mathbf{c}_{nmk}\Delta t, t + \Delta t) = \rho'_{nmk}(\mathbf{x}, t). \tag{2.8}$$

Combining (2.7) and (2.8), we obtain the complete LB particle dynamics,

$$\rho_{nmk}(\mathbf{x} + \mathbf{c}_{nmk}\Delta t, t + \Delta t) = \rho_{nmk}(\mathbf{x}, t) - \lambda\Delta t(\rho_{nmk}(\mathbf{x}, t) - \rho^{eq}_{nmk}(\mathbf{x}, t)), \tag{2.9}$$

in the case of no forcing.

We take the lattice spacing, Δx and Δz, as given. Then the dynamics (2.9) involves the 2 unspecified constants Δt and λ, and the 15 unspecified functions $\{\rho^{eq}_{nmk}(\rho, \mathbf{v})\}$. (Recall that $c_h = \Delta x/\Delta t$ and $c_v = \Delta z/\Delta t$.) We choose these constants and functions so that (2.9) approximate (2.1). As we shall see, the approximation is close if the time step Δt is relatively small, and if the decay coefficient λ is relatively large. If we regard c_h and c_v as fixed, then small Δt implies small Δx and Δz. Thus the limit $\Delta t \to 0$ corresponds to the limit of perfect resolution in time and space. On the other hand, large λ corresponds to ρ_{nmk} very close to ρ^{eq}_{nmk}. As we shall see, this limit corresponds to small viscosity.

Following Qian *et al.* (1992) and Chen *et al.* (1992) (see also He and Luo (1997)), we define the equilibrium densities as

$$\rho^{eq}_{nmk} = A_{nmk}\rho + B_{nmk}\left(n\frac{u}{c_h} + m\frac{v}{c_h} + k\frac{w}{c_v}\right), \tag{2.10}$$

where

$$A_{000} = 2/9, \tag{2.11}$$

for the rest particle ($n = m = k = 0$);

$$A_{nmk} = 1/9, \qquad B_{nmk} = 1/3 \tag{2.12}$$

for the 6 particles with $|n| + |m| + |k| = 1$ moving parallel to a coordinate axis; and

$$A_{nmk} = 1/72, \qquad B_{nmk} = 1/24 \tag{2.13}$$

for the 8 particles with $|n| + |m| + |k| = 3$ moving diagonally. The equilibrium state defined by (2.10–13) satisfies the important conditions

$$\sum_{nmk} \rho^{eq}_{nmk} = \sum_{nmk} \rho_{nmk} = \rho \tag{2.14}$$

and

$$\sum_{nmk} \mathbf{c}_{nmk} \rho^{eq}_{nmk} = \sum_{nmk} \mathbf{c}_{nmk} \rho_{nmk} = \mathbf{v}, \tag{2.15}$$

corresponding to the conservation of mass and momentum, respectively, by the collisions. As we shall see, the properties (2.14–15) are required for LB dynamics to approximate (2.1) at leading order. For future use, we note that (2.10–13) imply that

$$P_{\alpha\beta} \equiv \sum_{nmk} c_{nmk,\alpha} c_{nmk,\beta} \rho^{eq}_{nmk} \tag{2.16}$$

vanishes unless $\alpha = \beta$, and that

$$P_{11} = P_{22} = \tfrac{1}{3} c_h^2 \rho \equiv p_h \qquad \text{and} \qquad P_{33} = \tfrac{1}{3} c_v^2 \rho \equiv p_v. \tag{2.17}$$

Here, $c_{nmk,\alpha} = \mathbf{c}_{nmk} \cdot \mathbf{e}_\alpha$, where $(\mathbf{e}_1, \mathbf{e}_2, \mathbf{e}_3) = (\mathbf{i}, \mathbf{j}, \mathbf{k})$. In general, $\Delta x \neq \Delta z$, hence $c_h \neq c_v$, and thus the horizontal pressure p_h is unequal to the vertical pressure p_v; this requires a compensating adjustment as the derivation proceeds.

We investigate the particle dynamics (2.9) by means of an expansion—the Chapman-Enskog expansion—in which the small parameters are Δt and $\varepsilon \equiv \lambda^{-1}$. Once again, the smallness of Δt corresponds to slow variation on the scale of the time step and the lattice spacing. The smallness of ε corresponds to ρ_{nmk} very near the local equilibrium state ρ^{eq}_{nmk}. Thus we expand

$$\rho_{nmk} = \rho^{eq}_{nmk} + \varepsilon \rho^{(1)}_{nmk} + \varepsilon^2 \rho^{(2)}_{nmk} + \cdots \tag{2.18}$$

Expanding (2.9) in Δt, we obtain

$$\left(D_{nmk} + \frac{1}{2} \Delta t D^2_{nmk} + \cdots \right) \rho_{nmk} = -\frac{1}{\varepsilon} (\rho_{nmk} - \rho^{eq}_{nmk}), \tag{2.19}$$

where

$$D_{nmk} \equiv \frac{\partial}{\partial t} + \mathbf{c}_{nmk} \cdot \nabla_3 \tag{2.20}$$

is the advection operator in the direction of the *nmk*-th particle. Then, substituting (2.18) into (2.19), and assuming that Δt and ε have the same small size, we obtain

$$\Gamma^{(0)}_{nmk} + \Gamma^{(1)}_{nmk} + \cdots = 0, \tag{2.21}$$

where

$$\Gamma^{(0)}_{nmk} \equiv D_{nmk}\rho^{eq}_{nmk} + \rho^{(1)}_{nmk} \tag{2.22}$$

contains all the leading order terms, and

$$\Gamma^{(1)}_{nmk} \equiv \tfrac{1}{2}\Delta t D^2_{nmk}\rho^{eq}_{nmk} + \varepsilon D_{nmk}\rho^{(1)}_{nmk} + \varepsilon\rho^{(2)}_{nmk} \tag{2.23}$$

contains all the terms of order Δt or ε.

We obtain evolution equations for ρ and $\mathbf{v}$ by applying Σ_{nmk} and $\Sigma_{nmk}\mathbf{c}_{nmk}$ to (2.21). First note that (2.14–15) and (2.18) imply

$$\sum_{nmk}\rho^{(1)}_{nmk} = \sum_{nmk}\rho^{(2)}_{nmk} = \sum_{nmk}\mathbf{c}_{nmk}\rho^{(1)}_{nmk} = \sum_{nmk}\mathbf{c}_{nmk}\rho^{(2)}_{nmk} = 0. \tag{2.24}$$

By (2.14–17, 24),

$$\sum_{nmk}\Gamma^{(0)}_{nmk} = \frac{\partial\rho}{\partial t} + \nabla_3\cdot\mathbf{v} \tag{2.25}$$

and

$$\sum_{nmk}\mathbf{c}_{nmk}\Gamma^{(0)}_{nmk} = \frac{\partial\mathbf{v}}{\partial t} + \left(\frac{\partial p_h}{\partial x}, \frac{\partial p_h}{\partial y}, \frac{\partial p_v}{\partial z}\right). \tag{2.26}$$

Thus, at leading order, the dynamics (2.9) is equivalent to

$$\begin{aligned} \frac{\partial\rho}{\partial t} + \nabla_3\cdot\mathbf{v} &= 0 \\ \frac{\partial\mathbf{v}}{\partial t} &= -\left(\frac{\partial\phi}{\partial x}, \frac{\partial\phi}{\partial y}, \delta^2\frac{\partial\phi}{\partial z}\right) \end{aligned} \tag{2.27}$$

where

$$\phi \equiv p_h = \tfrac{1}{3}c_h^2\rho, \tag{2.28}$$

and

$$\delta \equiv \frac{c_v}{c_h} = \frac{\Delta z}{\Delta x} \tag{2.29}$$

is the aspect ratio based on the mesh size.

Typically δ is very small. According to (2.27b), small δ artificially reduces the vertical component of the pressure gradient. This artificial reduction occurs because, when $c_v \ll c_h$, particles move vertically at a speed much smaller than their horizontal speed, and therefore the momentum transferred by collisions to a horizontal wall immersed in the fluid—the vertical pressure—is much smaller than the momentum that would be transferred to a vertical wall. To compensate for the artificially small vertical pressure gradient, we shall

reduce the buoyancy (and other vertical forces, if present) by the same factor of δ^2. For now we continue with the analysis of (2.9).

The LB dynamics (2.9) implies a dissipation of momentum that appears at the next order of the Chapman-Enskog expansion. The steps leading to the following results are given in Appendix A. We find that, to consistent order,

$$\sum_{nmk} \Gamma^{(1)}_{nmk} = 0 \tag{2.30}$$

and

$$\sum_{nmk} \mathbf{c}_{nmk}\Gamma^{(1)}_{nmk} = -\left(\varepsilon - \frac{\Delta t}{2}\right)\frac{1}{3}(c_h^2\nabla^2\mathbf{v} + c_v^2\mathbf{v}_{zz} - c_h^2\nabla\rho_t - c_v^2\mathbf{k}\rho_{zt}). \tag{2.31}$$

Here and below, subscripts x, y, z and t denote partial derivatives. It follows from (2.30) that the continuity equation (2.27a) holds to the first *two* orders in Δt and ε. To the same order of accuracy, (2.27b) and (2.31) imply that

$$\begin{aligned}\frac{\partial \mathbf{u}}{\partial t} &= -\nabla\phi + A_h\nabla^2\mathbf{u} + A_v\mathbf{u}_{zz} - A\nabla\phi_t \\ \frac{\partial w}{\partial t} &= -\delta^2\phi_z + A_h\nabla^2 w + A_v w_{zz} - \delta^2 A\phi_{zt}\end{aligned} \tag{2.32}$$

where

$$(A, A_h, A_v) \equiv \left(\frac{1}{\lambda} - \frac{\Delta t}{2}\right)\left(1, \frac{c_h^2}{3}, \frac{c_v^2}{3}\right) \tag{2.33}$$

and we have used (2.28) to eliminate ρ in favor of ϕ. From (2.33) we see that the viscosity decreases with increasing λ, vanishing at the critical value $\lambda_{\max} = 2/\Delta t$. Still larger λ leads to instability in the form of negative viscosity coefficients. The last two terms in (2.32a, b) have no obvious physical interpretation. As we shall see in Section 5, these terms are negligible if the time step is sufficiently small.

3. Buoyancy

To accommodate buoyancy, we must introduce buoyancy particles. For reasons to be explained, we require only 6 buoyancy particles. Each buoyancy particle moves in 1 of the 6 directions parallel to a coordinate axis. Refer again to Figure 1. Thus

$$\begin{aligned}&\mathbf{c}_1 = (c_h, 0, 0), \qquad \mathbf{c}_2 = (0, c_h, 0), \qquad \mathbf{c}_3 = (-c_h, 0, 0), \\ &\mathbf{c}_4 = (0, -c_h, 0), \qquad \mathbf{c}_5 = (0, 0, c_v), \qquad \mathbf{c}_6 = (0, 0, -c_v)\end{aligned} \tag{3.1}$$

is the set of buoyancy-particle velocities. There is no rest particle for buoyancy.

Let $\theta_i(\mathbf{x}, t)$ be the contribution of the i-th buoyancy particle to the buoyancy,

$$\theta(\mathbf{x}, t) = \sum_{i=1}^{6} \theta_i(\mathbf{x}, t). \tag{3.2}$$

Like the mass particle dynamics (2.9), the buoyancy particle dynamics,

$$\theta_i(\mathbf{x} + \mathbf{c}_i\Delta t, t + \Delta t) = \theta_i(\mathbf{x}, t) - \Lambda\Delta t(\theta_i(\mathbf{x}, t) - \theta_i^{eq}(\mathbf{x}, t)), \tag{3.3}$$

comprises a streaming step and a collision step in which each θ_i relaxes, with relaxation coefficient Λ, toward its local equilibrium state θ_i^{eq}. The definition

$$\theta_i^{eq} = \frac{1}{6}\theta + \frac{1}{2\mathbf{c}_i^2}\mathbf{c}_i \cdot \mathbf{v}\theta \tag{3.4}$$

satisfies

$$\sum_i \theta_i^{eq} = \sum_i \theta_i = \theta \tag{3.5}$$

and

$$\sum_i \mathbf{c}_i\theta_i^{eq} = \mathbf{v}\theta. \tag{3.6}$$

Note, however, that

$$\sum_i \mathbf{c}_i\theta_i^{eq} \neq \sum_i \mathbf{c}_i\theta_i. \tag{3.7}$$

The asymmetry between (3.7) and (2.15) corresponds to the fact that the velocity **v** is defined by (2.6) as a mass-weighted—not a buoyancy-weighted—average. Because of this asymmetry, a diffusivity term appears in the evolution equation for θ, but not in the evolution equation (2.27a) for ρ.

To investigate (3.3), we apply the Chapman-Enskog expansion again, and sum (3.3) over *i*. The details are given in Appendix B. To the first *two* orders in the Chapman-Enskog expansion, the result is

$$\frac{\partial\theta}{\partial t} + \nabla_3 \cdot (\mathbf{v}\theta) = \kappa_h\nabla^2\theta + \kappa_v\theta_{zz} + \kappa\nabla_3 \cdot \frac{\partial}{\partial t}(\theta\mathbf{v}), \tag{3.8}$$

where

$$(\kappa, \kappa_h, \kappa_v) \equiv \left(\frac{1}{\Lambda} - \frac{\Delta t}{2}\right)\left(1, \frac{c_h^2}{3}, \frac{c_v^2}{3}\right). \tag{3.9}$$

Just as λ controls the viscosity in (2.32), Λ controls the diffusivity in (3.8). The last term in (3.8) is analogous to the last two terms in (2.32).

We defer discussion of the full, time-dependent LB dynamics until Section 5. Here we note that in steady state, (2.27a), (2.32) and (3.8) reduce to

$$\begin{aligned} \nabla_3 \cdot \mathbf{v} &= 0 \\ 0 &= -\nabla\phi + A_h\nabla^2\mathbf{u} + A_v\mathbf{u}_{zz} \\ 0 &= -\delta^2\phi_z + A_h\nabla^2 w + A_v w_{zz} \\ \mathbf{v} \cdot \nabla_3\theta &= \kappa_h\nabla^2\theta + \kappa_v\theta_{zz}. \end{aligned} \tag{3.10}$$

Thus we obtain a buoyancy equation (3.10d) of the correct form with only 6 buoyancy particles, whereas 15 mass particles were required to obtain the desired momentum equations. This difference arises from the different mathematical character of buoyancy and velocity. The buoyancy is a scalar whose flux, a vector, is accurately represented by a weighted sum of the buoyancy velocities $\mathbf{c}_i$. On the other hand, the velocity is a vector whose flux, a dyad formed from the products of the mass velocities $\mathbf{c}_{nmk}$, requires diagonally directed $\mathbf{c}_{nmk}$ for its accurate representation.

The steady dynamics (3.10) differs from (2.1) in the absence of buoyancy and Coriolis force, and in the factor δ^2 preceding the vertical derivative of pressure. We can add the buoyancy force by the general method of the following section. Instead, we prefer to build the buoyancy force into the definition of the local equilibrium state. Let the definition of ρ^{eq}_{nmk} for the 3 mass particles with $n = m = 0$ be changed from (2.10–13) to

$$\begin{aligned} \rho^{eq}_{000} &= \frac{2}{9}\rho + b \\ \rho^{eq}_{001} &= \frac{1}{9}\rho + \frac{w}{3c_v} - \frac{b}{2} \\ \rho^{eq}_{00\text{-}1} &= \frac{1}{9}\rho - \frac{w}{3c_v} - \frac{b}{2} \end{aligned} \tag{3.11}$$

where b is a functional of θ to be determined. When $b = 0$, (3.11) reduce to (2.10). When $b \neq 0$, the conservation laws (2.14–15) are unchanged. Thus the continuity equation (2.27a) still holds to the first two orders in the Chapman-Enskog expansion. The horizontal pressure (2.28) is also unchanged, but the vertical pressure

$$P_{33} = \tfrac{1}{3}c_v^2\rho - c_v^2 b = \delta^2\phi - \delta^2 c_h^2 b \tag{3.12}$$

acquires a term proportional to b. If we define

$$b(x, y, z, t) \equiv \frac{1}{c_h^2}\int^z \theta(x, y, z', t)\, dz', \tag{3.13}$$

then the leading-order momentum equation (2.27b) acquires the buoyancy term $\delta^2\theta\mathbf{k}$ on its right-hand side. At next order, $b \neq 0$ contributes an additional term; for details see Appendix C. We find that, to the first two orders in the Chapman-Enskog expansion, the vertical momentum equation generalizes from (2.32b) to

$$\frac{\partial w}{\partial t} = -\delta^2\frac{\partial \phi}{\partial z} + \delta^2\theta + A_h\nabla^2 w + A_v w_{zz} - \delta^2 A(\theta_t + \phi_{zt}). \tag{3.14}$$

The last two terms in (3.14) are terms like the time-derivative terms on the right-hand sides of (2.32) and (3.8). We discuss all these terms in Section 5, where we consider properties of the full, time-dependent LB equations. But first, in the following section, we incorporate the Coriolis, wind, and diabatic forcing.

4. Forcing

Let $\mathbf{F}(\mathbf{x}, t)$ be a general horizontal force (per unit mass).[3] We incorporate $\mathbf{F}$ into LB dynamics by inserting an *impulse step* on each side of the streaming step. Each impulse step consists of two parts. In the first part, we estimate the change $\Delta\mathbf{u}$ in the horizontal velocity caused by $\mathbf{F}$ acting for a time $\Delta t/2$. In the second part of the impulse step, we distribute this impulse among the particles. That is, we replace ρ_{nmk} by

$$\rho'_{nmk} = \rho_{nmk} + \frac{B_{nmk}}{c_h^2}\mathbf{c}_{nmk}\cdot\Delta\mathbf{u} = \rho_{nmk} + \frac{B_{nmk}}{c_h}(n\Delta u + m\Delta v), \tag{4.1}$$

where B_{nmk} is given by (2.12–13), and the prime denotes the value immediately after the impulse step. Using (2.4), (2.6), and (2.12–13) it is easy to see that the horizontal velocity corresponding to ρ'_{nmk} differs from that corresponding to ρ_{nmk} by the amount $\Delta\mathbf{u}$.[4]

To ensure the required second-order accuracy in the Chapman-Enskog expansion, the composite *impulse-stream-impulse* step must be equivalent to a second-order accurate solution of

$$\left(\frac{\partial}{\partial t} + \mathbf{c}_{nmk}\cdot\nabla\right)\rho_{nmk} = \frac{B_{nmk}}{c_h^2}\mathbf{c}_{nmk}\cdot\mathbf{F}. \tag{4.2}$$

A discrete algorithm having this property is

$$\begin{aligned}\rho_{nmk}(\mathbf{x} + \mathbf{c}_{nmk}\Delta t, t + \Delta t) = \rho_{nmk}(\mathbf{x}, t) + \Delta t\frac{B_{nmk}}{c_h^2}\mathbf{c}_{nmk}\\ \cdot\left[\frac{1}{2}\mathbf{F}(\mathbf{x} + \mathbf{c}_{nmk}\Delta t, t + \Delta t) + \frac{1}{2}\mathbf{F}(\mathbf{x}, t)\right].\end{aligned} \tag{4.3}$$

To see that (4.3) yields the correct result, we first expand (4.3) in Δt, obtaining

$$\begin{aligned}\left(\Delta t D_{nmk} + \frac{1}{2}(\Delta t)^2 D_{nmk}^2 + \cdots\right)\rho_{nmk}(\mathbf{x}, t)\\ = \Delta t\frac{B_{nmk}}{c_h^2}\mathbf{c}_{nmk}\cdot\left[\mathbf{F}(\mathbf{x}, t) + \frac{1}{2}\Delta t D_{nmk}\mathbf{F}(\mathbf{x}, t) + \cdots\right].\end{aligned} \tag{4.4}$$

From (4.4) we see that the presence of $\mathbf{F}$ generalizes (2.22) to

$$\Gamma^{(0)}_{nmk} = D_{nmk}\rho^{eq}_{nmk} + \rho^{(1)}_{nmk} - \frac{B_{nmk}}{c_h^2}\mathbf{c}_{nmk}\cdot\mathbf{F}, \tag{4.5}$$

3. Although, the discussion is easily generalized to include vertical forces, we require only horizontal forces.

4. As this is the only property required, (4.1) is somewhat arbitrary, but it seems best to distribute the momentum using the same weights as in the definition (2.10) of the equilibrium states.

and (2.23) to

$$\Gamma^{(1)}_{nmk} = \frac{\Delta t}{2} D^2_{nmk} \rho^{eq}_{nmk} + \varepsilon D_{nmk} \rho^{(1)}_{nmk} + \varepsilon \rho^{(2)}_{nmk} - \frac{\Delta t}{2} \frac{B_{nmk}}{c_h^2} D_{nmk} (\mathbf{c}_{nmk} \cdot \mathbf{F}). \tag{4.6}$$

By carefully repeating the steps in Section 2 and Appendix A for the more general case $\mathbf{F} \neq 0$, we find no other change than the appearance of $\mathbf{F}$ on the right-hand side of the horizontal momentum equation (2.32a).

If the horizontal force $\mathbf{F}$ can be prescribed, as if $\mathbf{F}$ is actually steady (like the wind stress in the solutions described in Section 6), then it is very easy to use the algorithm (4.3). However, if $\mathbf{F}$ depends upon the flow itself, so that the right-hand side of (4.3) depends on ρ_{nmk} at the new time $t + \Delta t$, then the formula (4.3) is implicit and therefore very difficult to satisfy exactly. Unfortunately, the Coriolis force, $\mathbf{F} = -f\mathbf{k} \times \mathbf{u}$, is such a force. Despite this, S99 incorporated the Coriolis force into shallow-water LB dynamics by using a predictor-corrector approximation to the analog of (4.3). However, the predictor-corrector method is unaesthetic and required too many correctors for the present three-dimensional application. Here we show the method of inserting a Coriolis impulse on each side of the streaming step to be a superior alternative. Since this is a new result of great practical importance, we give the full details.

In each Coriolis impulse step, we compute the change

$$\Delta u_\alpha = A_{\alpha\beta} u_\beta \tag{4.7}$$

in the horizontal velocity caused by Coriolis force acting for a half time step. Here, Greek subscripts denote directional components, repeated Greek subscripts are summed from 1 to 2, and the matrix $A_{\alpha\beta}$ is defined by

$$[A_{\alpha\beta}] = \begin{bmatrix} \cos\left(\frac{f\Delta t}{2}\right) - 1 & \sin\left(\frac{f\Delta t}{2}\right) \\ -\sin\left(\frac{f\Delta t}{2}\right) & \cos\left(\frac{f\Delta t}{2}\right) - 1 \end{bmatrix} = \frac{f\Delta t}{2} \varepsilon_{\alpha\beta} - \frac{(f\Delta t)^2}{8} \delta_{\alpha\beta} + \cdots \tag{4.8}$$

where $\varepsilon_{\alpha\beta}$ is the permutation symbol and $\delta_{\alpha\beta}$ the Kronecker delta. The velocity on the right-hand side of (4.7) is the velocity *before* the impulse step.

We distribute the impulse (4.7) among the particles by substituting (4.7) into (4.1). The result is

$$\rho'_{nmk}(\mathbf{x}, t) = \rho_{nmk}(\mathbf{x}, t) + \frac{B_{nmk}}{c_h^2} c_{nmk,\alpha} A_{\alpha\beta} u_\beta(\mathbf{x}, t), \tag{4.9}$$

where $c_{nmk,\alpha} = \mathbf{c}_{nmk} \cdot \mathbf{e}_\alpha$, and the prime denotes the particle density immediately after the impulse. The Coriolis impulse (4.9) is followed by the streaming step,

$$\rho''_{nmk}(\mathbf{x} + \mathbf{c}_{nmk}\Delta t, t + \Delta t) = \rho'_{nmk}(\mathbf{x}, t), \tag{4.10}$$

and the other Coriolis impulse,

$$\rho'''_{nmk}(\mathbf{x}, t) = \rho''_{nmk}(\mathbf{x}, t) + \frac{B_{nmk}}{c_h^2} c_{nmk,\alpha} A_{\alpha\beta} u''_\beta(\mathbf{x}, t). \tag{4.11}$$

Here, double primes denote the state immediately after the streaming step, and triple primes denote the state after the second Coriolis impulse. The full LB cycle comprises the three steps (4.9–11) followed (or preceded) by the collision step. Unlike (4.3), the 3 steps (4.9–11) are explicit; the velocities on the right-hand sides of (4.9) and (4.11) are computed from the results of the previous equation.

We must show that the three steps (4.9–11) are together equivalent to (4.3) or (4.4) with the required second order accuracy. We proceed by back-substitution from (4.11). After the second Coriolis impulse, the densities are given by (4.11) in the form

$$\begin{aligned}\rho_{nmk}(\mathbf{x} + \mathbf{c}_{nmk}\Delta t, t + \Delta t) &= \rho''_{nmk}(\mathbf{x} + \mathbf{c}_{nmk}\Delta t, t + \Delta t) \\ &+ \frac{B_{nmk}}{c_h^2} c_{nmk,\alpha} A_{\alpha\beta}(\mathbf{x} + \mathbf{c}_{nmk}\Delta t, t + \Delta t) \sum_{rsp} c_{rsp,\beta} \rho''_{rsp}(\mathbf{x} + \mathbf{c}_{nmk}\Delta t, t + \Delta t).\end{aligned} \tag{4.12}$$

Substituting from (4.10), this is

$$\begin{aligned}\rho_{nmk}(\mathbf{x} + \mathbf{c}_{nmk}\Delta t, t + \Delta t) &= \rho'_{nmk}(\mathbf{x}, t) \\ &+ \frac{B_{nmk}}{c_h^2} c_{nmk,\alpha} A_{\alpha\beta}(\mathbf{x} + \mathbf{c}_{nmk}\Delta t, t + \Delta t) \sum_{rsp} c_{rsp,\beta} \rho'_{rsp}(\mathbf{x} + \mathbf{c}_{nmk}\Delta t - \mathbf{c}_{rsp}\Delta t, t).\end{aligned} \tag{4.13}$$

Finally, substituting from (4.9) and using (2.6) we obtain

$$\begin{aligned}&\rho_{nmk}(\mathbf{x} + \mathbf{c}_{nmk}\Delta t, t + \Delta t) \\ &\quad = \rho_{nmk}(\mathbf{x}, t) + \frac{B_{nmk}}{c_h^2} c_{nmk,\alpha} A_{\alpha\beta}(\mathbf{x}, t) \sum_{rsp} c_{rsp,\beta} \rho_{rsp}(\mathbf{x}, t) \\ &\qquad + \frac{B_{nmk}}{c_h^2} c_{nmk,\alpha} A_{\alpha\beta}(\mathbf{x} + \mathbf{c}_{nmk}\Delta t, t + \Delta t) \sum_{rsp} c_{rsp,\beta} \\ &\times \left\{ \rho_{rsp}(\mathbf{x} + (\mathbf{c}_{nmk} - \mathbf{c}_{rsp})\Delta t, t) + \frac{B_{rsp}}{c_h^2} c_{rsp,\gamma} A_{\gamma\delta}(\mathbf{x} + (\mathbf{c}_{nmk} - \mathbf{c}_{rsp})\Delta t, t) \right. \\ &\qquad \left. \times \sum_{abd} c_{abd,\delta} \rho_{abd}(\mathbf{x} + (\mathbf{c}_{nmk} - \mathbf{c}_{rsp})\Delta t, t) \right\}\end{aligned} \tag{4.14}$$

Eq (4.14) relates the particle densities after the second Coriolis impulse to the densities before the first impulse. In Appendix D we show that, to the required second order accuracy, (4.14) is equivalent to (4.4) with $\mathbf{F} = -f\mathbf{k} \times \mathbf{u}$. This proves that the Coriolis impulse algorithm yields the desired Coriolis force when the Chapman-Enskog expansion is applied.

To incorporate a prescribed diabatic heating Q, we distribute the buoyancy amount $Q \times \Delta t/2$ among the 6 buoyancy particles before and after each streaming step. That is, we add

$Q \times \Delta t/12$ to each θ_i. It is easy to show that this corresponds to the addition of Q to the right-hand side of the buoyancy equation, (3.8) or (3.10c).

5. Properties of the lattice Boltzmann model

First we summarize the lattice Boltzmann model as an algorithm with a 6-step cycle:

[1] At every lattice point, compute the macroscopic variables

$$\begin{aligned} \rho(\mathbf{x}, t) &= \sum_{n,m,k} \rho_{nmk}(\mathbf{x}, t) \\ \mathbf{v}(\mathbf{x}, t) &= \sum_{n,m,k} \mathbf{c}_{nmk}\rho_{nmk}(\mathbf{x}, t) \\ \theta(\mathbf{x}, t) &= \sum_{i} \theta_i \end{aligned} \tag{5.1}$$

where $\mathbf{c}_{nmk}$ is defined by (2.4). The nmk-summation is over the 15-member set of mass particles, and the i-summation is over the 6-member set of buoyancy particles.

[2] Compute the local equilibrium states

$$\rho^{eq}_{nmk} = A_{nmk}\rho + B_{nmk}\left(n\frac{u}{c_h} + m\frac{v}{c_h} + k\frac{w}{c_v}\right) + \delta_{n0}\delta_{m0}\begin{cases} b, & k = 0 \\ -\tfrac{1}{2}b, & k = \pm 1 \end{cases} \tag{5.2}$$

and

$$\theta^{eq}_i = \frac{1}{6}\theta + \frac{1}{2\mathbf{c}_i^2}\mathbf{c}_i \cdot \mathbf{v}\theta, \tag{5.3}$$

where the coefficients A_{nmk} and B_{nmk} are given by (2.10–13), b by (3.13), and the buoyancy particle velocities $\mathbf{c}_i$ by (3.1).

[3] Collide the particles,

$$\begin{aligned} \rho_{nmk} &\leftarrow \rho_{nmk} - \lambda\Delta t(\rho_{nmk} - \rho^{eq}_{nmk}) \\ \theta_i &\leftarrow \theta_i - \Lambda\Delta t(\theta_i - \theta^{eq}_i) \end{aligned} \tag{5.4}$$

[4] Apply impulses representing the action of horizontal forcing and heating for a time interval of $\Delta t/2$,

$$\rho_{nmk} \leftarrow \rho_{nmk} + \frac{\Delta t B_{nmk}}{2c_h}(n\Delta u + m\Delta v) \tag{5.5}$$

$$\theta_i \leftarrow \theta_i + \frac{\Delta t}{12}Q. \tag{5.6}$$

Here, $\Delta\mathbf{u}$, the change in the horizontal velocity caused by the force, is given by (4.7–8) for the case of Coriolis force. Q is the diabatic heating.

[5] Stream the particles,

$$\begin{aligned} \rho_{nmk}(\mathbf{x} + \mathbf{c}_{nmk}\Delta t, t + \Delta t) &= \rho_{nmk}(\mathbf{x}, t) \\ \theta_i(\mathbf{x} + \mathbf{c}_i\Delta t, t + \Delta t) &= \theta_i(\mathbf{x}, t) \end{aligned} \tag{5.7}$$

[6] Apply step 4 again.

[7] Return to step 1.

Thus the LB algorithm corresponds to a computer code with a half dozen simple loops. The boundary conditions correspond to modifications of the streaming step (5.7) near the boundaries, and will be discussed in Section 6.

As shown in Sections 2–4 and in the appendices, to the first 2 orders in Δt, λ^{-1} and Λ^{-1}, the algorithm (5.1–7) is equivalent to the following set of differential equations:

$$\begin{aligned}
&\frac{\partial \phi}{\partial t} + c_s^2 \nabla_3 \cdot \mathbf{v} = 0 \\
&\frac{\partial \mathbf{u}}{\partial t} + f\mathbf{k} \times \mathbf{u} = -\nabla\phi + A_h \nabla^2 \mathbf{u} + A_v \mathbf{u}_{zz} + \mathbf{F} - A\nabla\phi_t \\
&\qquad \delta^{-2} \frac{\partial w}{\partial t} = -\frac{\partial \phi}{\partial z} + \theta + \delta^{-2} A_h \nabla^2 w + \delta^{-2} A_v w_{zz} - A(\theta_t + \phi_{zt}) \\
&\frac{\partial \theta}{\partial t} + \nabla_3 \cdot (\mathbf{v}\theta) = \kappa_h \nabla^2 \theta + \kappa_v \theta_{zz} + Q + \kappa \nabla_3 \cdot (\theta \mathbf{v})_t
\end{aligned} \tag{5.8}$$

where

$$c_s^2 \equiv \tfrac{1}{3} c_h^2, \tag{5.9}$$

and we have used (2.28) to eliminate ρ. In (5.8), $\mathbf{F}$ is the external forcing and Q is the diabatic heating. The viscosity and diffusion coefficients are given by (2.33) and (3.9). It is easily shown that c_s is the speed of "sound waves" in the horizontal direction; the sound waves travel vertically at speed δc_s. These sound waves are artificial in the sense that their speed is determined by the arbitrarily prescribed particle velocities, c_h and c_v, and not by an imposed equation of state. As we shall see, the prescribed particle velocities must, for sake of numerical stability, exceed the velocities of gravity waves and macroscopic fluid particles but they need not be as great as the speed of real sound waves.

Our numerical experiments show that, if the forcing and heating are steady, then the solutions of the LB equations approach a quasi-steady state. Hence, the most important property of the LB dynamics is that, in steady state, (5.8) reduce to

$$\begin{aligned}
\nabla_3 \cdot \mathbf{v} &= 0 \\
f\mathbf{k} \times \mathbf{u} &= -\nabla\phi + A_h \nabla^2 \mathbf{u} + A_v \mathbf{u}_{zz} \\
0 &= -\phi_z + \theta + \delta^{-2}(A_h \nabla^2 w + A_v w_{zz}) \\
\mathbf{v} \cdot \nabla_3 \theta &= \kappa_h \nabla^2 \theta + \kappa_v \theta_{zz}
\end{aligned} \tag{5.10}$$

which differs from (2.1) only in the presence of the large dimensionless factor δ^{-2} in the w-viscosity. (To simplify the discussion, we once again temporarily omit the external forcing and heating terms.) That is, insofar as steady solutions are concerned, the only

effect of the compromises required to formulate planetary geostrophic dynamics as a lattice Boltzmann model is the artificially enhanced w-viscosity in (5.10c). As we have seen, this large w-viscosity results from the typically very small ratio $\delta = \Delta z/\Delta x$ between the vertical and horizontal lattice spacing. Now, making virtue out of necessity, we argue that this large w-viscosity is exactly what is needed to resolve the sidewall frictional boundary layers that occur in solutions of (5.10).

Suppose that (5.10) are made nondimensional using the same scalings as for (2.1). Suppose further that $\delta_b = \delta$, where, as in Section 2, $\delta_b \equiv H/L$ is the aspect ratio based on the ocean basin dimensions. Then the nondimensional form of (5.10) differs from the nondimensional form (2.2) of (2.1) only in the *disappearance* of the δ_b^2-factor in the w-viscosity. That is, the δ^{-2}-factor in (5.10) cancels out the δ_b^2-factor that appears in (2.2c). Thus, in steady LB dynamics (5.10), viscous departures from hydrostatic balance can be as large as the viscous departures from geostrophic balance. Whether this is wanted or not, it seems to be necessary if we mean to resolve all the viscous boundary layers. Unresolved boundary layers typically cause spurious oscillations and large errors in the solutions.

In classic papers, Pedlosky (1968, 1969) explored the boundary layer structure of the *linearized* form of (2.2). In the case of homogeneous fluid (Pedlosky, 1968), if $\delta_b \ll E_h^{1/3}$, then there are 3 nested, longitudinal boundary layers with the thicknesses $E_h^{1/3}$, $E_h^{1/2}$, and δ_b. The thickest, $E_h^{1/3}$-layer is the Munk layer. The thinnest, δ_b-layer is nonhydrostatic. However, if $\delta_b \ll E_h^{1/3}$, then it is practically impossible to resolve this thinnest boundary layer in a numerical model. On the other hand, if $\delta_b \gg E_h^{1/3}$—and, once again, the LB model effectively sets $\delta_b = 1$—then the three boundary layers coalesce into a *single* nonhydrostatic boundary layer of thickness $E_h^{1/3}$, which is easy to resolve.

In the nonhomogeneous (stratified) case (Pedlosky, 1969), the value of δ_b seems almost irrelevant, but linear stratified theory, which assumes that the mean buoyancy is independent of horizontal location, bears a very problematic relation to solutions of the full, nonlinear, planetary geostrophic equations, in which horizontal variations of the buoyancy are as large as vertical variations, and large regions of the subpolar gyres are nearly homogeneous. Even in the stratified case, it seems intuitively clear that the effective assumption of unit aspect ratio by the LB model permits the use of approximately the same number of lattice points in the vertical and horizontal directions.

Of course, the conventional approach to ocean circulation modeling is to impose the condition of exact hydrostatic balance, and to determine the vertical velocity w from the condition $\nabla_3 \cdot \mathbf{v} = 0$ at all horizontal locations. In this approach, one loses the ability to prescribe sidewall boundary conditions on w, but the only elliptic equation requiring solution is two-dimensional. If the boundary condition on the horizontal velocity $\mathbf{u}$ is no-slip, this conventional approach produces the somewhat bizarre situation that particles move freely along the sidewall in the vertical direction only. In Section 6, we show that LB solutions with boundary conditions of no-stress (in both tangential directions) are globally hydrostatic despite the large viscosity in the vertical momentum equation, and therefore probably similar to solutions of the conventional equations.

Although primary interest attaches to steady final solutions satisfying (5.10), we now briefly consider the full, time-dependent LB dynamics (5.8). The full equations appear inconsistent in that they contain the local time-derivatives of momentum but omit its advection. However, we view these local time-derivative terms merely as a device for relaxing the velocity field to its quasi-steady equilibrium state. The equilibrium state is geostrophic and hydrostatic, apart from significant viscous boundary layer corrections. If the time-derivatives of velocity had been omitted, we would instead be solving elliptic equations to determine the velocity field. Time-stepping the velocity is analogous to solving these elliptic equations by a relaxation method, but the time-stepping strategy is simpler and more physically appealing.[5] In particular, linear wave solutions of (5.8) resemble the wave solutions of the linearized primitive equations.

The primary differences between (5.8) and the primitive equations are the presence of the compressibility term ϕ_t in (5.8a), the terms proportional to A and κ in (5.8b–d), and the $\theta\nabla_3 \cdot \mathbf{v}$ term in (5.8d). First we show that these unfamiliar terms are negligibly small in solutions that obey the standard scaling for large-scale, low-frequency ocean flow. Then we analyze these terms more closely, showing that they can lead to numerical instability, but only when the time step is relatively large.

If we apply the standard scaling described in Section 2 (with, additionally, time scaled by $T = L/U$), we obtain (5.8) in the nondimensional form

$$\begin{aligned}
\mu \frac{\partial \phi}{\partial t} + \nabla_3 \cdot \mathbf{v} &= 0 \\
Ro \frac{\partial \mathbf{u}}{\partial t} + f\mathbf{k} \times \mathbf{u} &= -\nabla\phi + E_h\nabla^2\mathbf{u} + E_v\mathbf{u}_{zz} - \mu E_h \nabla\phi_t \\
Ro \frac{\partial w}{\partial t} &= -\frac{\partial \phi}{\partial z} + \theta + E_h\nabla^2 w + E_v w_{zz} - \mu E_h(\theta_t + \phi_{zt}) \\
\frac{\partial \theta}{\partial t} + \nabla_3 \cdot (\mathbf{v}\theta) &= D_h\nabla^2\theta + D_v\theta_{zz} + D_h M^2 \nabla_3 \cdot (\theta\mathbf{v})_t
\end{aligned} \tag{5.11}$$

where $Ro \equiv U/f_0L$ is the Rossby number, $M \equiv U/c_s$ is the Mach number, $\mu \equiv M^2/Ro$, and the other parameters are defined in (2.3). Thus, if the Mach number is sufficiently small, all the terms proportional to μ or M in (5.11) are negligible, and $\nabla_3 \cdot (\mathbf{v}\theta) \approx \mathbf{v} \cdot \nabla_3\theta$. Then (5.11) take a familiar form, remarkable only for the absence of Reynolds stresses and for the absence of the δ^2-factor in the 3 w-terms of (5.11c); compare (2.2). For fixed lattice spacing, small Mach number corresponds to small time step. However, as we see next, numerical stability requirements *force* the Mach number to be small, thus virtually guaranteeing that the unphysical terms in (5.8) are negligible in the large-scale, low-frequency flow of interest.

5. Based on my experience, time-stepping is more stable and hardly less efficient than even sophisticated relaxation methods when the Ekman numbers are realistically small.

We begin our analysis of the time-dependent equations by noting that (5.8) imply an energy equation of the form,

$$\partial_t[\tfrac{1}{2}u^2 + \tfrac{1}{2}v^2 + \tfrac{1}{2}\delta^{-2}w^2 - z\theta + \tfrac{1}{2}c_s^{-2}\phi^2] = -\nabla_3 \cdot (\mathbf{v}\phi - \mathbf{v}z\theta) + D, \tag{5.12}$$

where

$$\begin{aligned} D = A_h\mathbf{u} \cdot \nabla^2\mathbf{u} + A_v\mathbf{u} \cdot \mathbf{u}_{zz} + \delta^{-2}(A_h w\nabla^2 w + A_v w w_{zz}) \\ - A\mathbf{v} \cdot \nabla_3\phi_t - Aw\theta_t - z\kappa_h\nabla^2\theta - z\kappa_v\theta_{zz} - z\kappa\nabla_3 \cdot (\theta\mathbf{v})_t \end{aligned} \tag{5.13}$$

contains all the terms arising at the second order of the Chapman-Enskog expansion. The vertical kinetic energy in (5.12) is enhanced by the expected factor of δ^{-2} and thus has the same size as the horizontal kinetic energy. The internal energy—the last term on the left-hand side of (5.12)—is insignificant if the Mach number is small, that is, if the particle speeds c_h and c_v are much larger than the corresponding fluid speeds.

The A-terms containing ϕ_t in (5.8b–c) and (5.13) are like those present in *compressible* Navier-Stokes theory. While the form of (5.8) emphasizes that these terms vanish in steady state, the $A\phi_t$-terms take a more familiar form if we eliminate ϕ_t by substitution from (5.8a). Then, as expected, all the terms not containing θ in (5.13) may be integrated by parts to yield a negative definite contribution to the spatial integral of D. On the other hand, the θ-terms proportional to A and κ in (5.8c–d) and (5.13) have no obvious physical interpretation. As we shall see, these terms cause instability if the time step is too large.

First, consider the κ-term in the buoyancy equation (5.8d). Once again, all the terms appearing on the right-hand side of (5.8d) arise at the second order of the Chapman-Enskog approximation. Therefore, we may consistently substitute from the leading order balance—the left-hand side of (5.8d)—to obtain the approximation

$$\kappa\nabla_3 \cdot \frac{\partial}{\partial t}(\theta\mathbf{v}) \approx -\kappa\theta_{tt}. \tag{5.14}$$

Thus, to consistent order, the buoyancy equation (5.8d) is equivalent to

$$\frac{\partial\theta}{\partial t} + \nabla_3 \cdot (\mathbf{v}\theta) = \kappa(-\theta_{tt} + c_s^2\nabla^2\theta + \delta^2 c_s^2\theta_{zz}) + Q \tag{5.15}$$

in which the "sound-wave operator"

$$-\partial_{tt} + c_s^2\nabla^2 + \delta^2 c_s^2\partial_{zz} \tag{5.16}$$

appears in place of the desired diffusivity. If, at leading order, $\theta \propto \exp(i\mathbf{k} \cdot \mathbf{x} - \omega t)$, where the frequency ω corresponds to any physical wave or fluid particle advection speed (e.g. $\omega = \mathbf{v} \cdot \mathbf{k}$), then the wave operator (5.16) is proportional to

$$\omega^2 - c_s^2 k_h^2 - \delta^2 c_s^2 k_v^2 \tag{5.17}$$

where k_h is the horizontal wavenumber and k_v the vertical wavenumber. If (5.17) is positive—that is, if the velocity of waves or fluid particles exceeds the sound speed—then the solution grows exponentially. The condition that (5.17) be negative is just the Courant-Lewy-Friedrichs (CLF) condition.

A similar conclusion applies to the $A\theta_t$-term in (5.8c). In the case of linear waves, $\theta_t \approx -wN^2$ at leading order, where N is the Vaisala frequency, and thus

$$\delta^{-2}A_h\nabla^2 w + \delta^{-2}A_v w_{zz} - A\theta_t = A\delta^{-2}c_s^2(\nabla^2 w + \delta^2 w_{zz}) + AN^2 w. \tag{5.18}$$

If $w \propto \exp(i\mathbf{k}\cdot\mathbf{x} - \omega t)$, this is proportional to

$$\delta^2 N^2 - c_s^2 k_h^2 - \delta^2 c_s^2 k_v^2. \tag{5.19}$$

Note that (5.19) corresponds to (5.17) with $\omega = \delta N$. Once again, numerical instability results if (5.19) is positive. However, (5.19) corresponds to the CLF criterion for internal waves with a (maximum) frequency of δN, with the δ-factor arising from the artificially enhanced vertical momentum—the δ^{-2}-factor in the first term of (5.8c). Thus the artificial enhancement of the vertical momentum produces a benefit as great as the corresponding enhancement of friction in the same equation, namely, the ability to take time steps much larger—by a factor of δ^{-1}—than in the conventional primitive equations.

All of these results are based upon (5.8). Since (5.8) rest upon the assumptions of small Δt, λ^{-1} and Λ^{-1} (via the Chapman-Enskog theory), it is somewhat dangerous to use (5.8) to infer limits on Δt. On the other hand, a direct stability analysis of the general algorithm (5.1–7) seems impossible. As with all complicated numerical algorithms, we must largely judge the algorithm by its results. This we do in the following section.

6. Numerical solutions

Now we examine solutions of the lattice Boltzmann model in a square ocean basin, $0 < x, y < L$, with side $L = 4000$ km and depth $H = 4$ km. We take $f = f_0 + \beta(y - L/2)$ where $f_0 = 2\pi$ day^{-1} and $\beta = f_0/6400$ km. All of the solutions described have 50^3 lattice points. Thus $\Delta x = 80$ km, $\Delta z = 80$ m, and $\delta_b = \delta$; both the basin and the lattice elements have the same aspect ratio. Then the remaining parameters of the model (besides the external forcing) are the time step Δt, and the relaxation coefficients λ and Λ.

For fixed lattice spacings, the time step determines $c_h = \Delta x/\Delta t$, $c_v = \Delta z/\Delta t$, and the sound speed $c_s = c_h/\sqrt{3}$. Once again, a large time step corresponds to a small sound speed, and numerical instability results if the sound speed becomes too small. In all the solutions described $c_h = 1000$ km day^{-1}; hence $\Delta t = \Delta x/c_h = 0.08$ days and $c_v = 1.0$ km day^{-1}. Experiments showed the results to be independent of the sound speed at speeds larger than this, but (even though numerical stability was maintained) a dependence on sound speed began to appear at lower speeds. Thus $\Delta t = 0.08$ days seems to be largest practicable time step. This is still many times larger than the maximum time step in conventional primitive equation models.

The relaxation coefficients control the viscosity and diffusivity. We choose the mass-particle relaxation coefficient λ by demanding that the western boundary layer, of thickness $(A_h/\beta)^{1/3}$, be 2 lattice spacings (160 km) wide. This leads to $A_h = 5 \times 10^8$ cgs, $A_v = \delta^2 A_h = 5 \times 10^2$ cgs, and $\lambda = 0.761\lambda_{\max}$, where $\lambda_{\max} = 2/\Delta t$.

We choose the buoyancy-particle relaxation coefficient Λ by specifying the vertical diffusion coefficient κ_v. Experiments showed that the smallest attainable κ_v depends strongly on the vertical resolution. For $\Delta z = 80$ km, as in all the solutions presented, the smallest attainable κ_v is 5 cgs, corresponding to $\kappa_h = \delta^{-2}\kappa_v = 5 \times 10^6$ cgs and $\Lambda = 0.997\ \Lambda_{\max}$. This is larger than the canonical value of $\kappa_v = 0.1$–1.0 cgs, but the results depend rather weakly on diffusivity; recall that the internal boundary layer corresponding to the main thermocline has a thickness varying as $\kappa_v^{1/2}$.[6] At 50^3 resolution, solutions with κ_v less than 5 cgs showed spurious oscillations in the midwater region of rapid vertical buoyancy variation with depth. Thus the need to resolve this internal boundary layer apparently determines the minimum value of diffusivity.

The solution is driven by wind forcing and diabatic heating. For the wind forcing we take

$$\mathbf{F} = \frac{1}{d} e^{z/d}(\tau_0, 0), \tag{6.1}$$

where $z = 0$ corresponds to the ocean surface, and

$$\tau_0(x, y) = 1.0\ \text{cm}^2\ \text{sec}^{-2} \sin^2(\pi y/L), \qquad 0 < y < L \tag{6.2}$$

is the eastward component of wind stress. Thus the wind momentum enters as a body force acting in a layer of constant thickness d near the ocean surface. In all the experiments discussed, $d = 2\Delta z = 160$ m. The wind stress (6.2) corresponds to a double gyre. This wind stress and its curl vanish at the northern and southern boundaries.

Of course, one could equally well model the wind stress as a momentum flux through the ocean surface, relying on the fluid viscosity for downward mixing in an Ekman layer of thickness of $(A_v/f_0)^{1/2}$. The advantage of the body-force approach (which, considering the special and very complicated nature of momentum mixing near the ocean surface, is at least equally defensible) is that the Ekman layers need not then be resolved. Indeed, the viscosity values given above imply an Ekman layer thickness of about 25 m, which is smaller than the vertical lattice spacing of 80 m. In all the experiments presented, we impose boundary conditions of no stress. For example, $u = w_x = v_x = 0$ at the western sidewall, and $w = u_z = v_z = 0$ at the ocean surface. In the LB model, these boundary conditions correspond to elastic collisions of the particles with the boundaries. If the interior ocean flow is smooth on the scale of the Ekman layers, then the interior flow satisfies the top and bottom boundary conditions by itself, and no Ekman layers are required at leading order. Other solutions (not presented) with no-slip or prescribed-flux

6. See, for example, Salmon, 1998, pp. 191–195, and references therein.

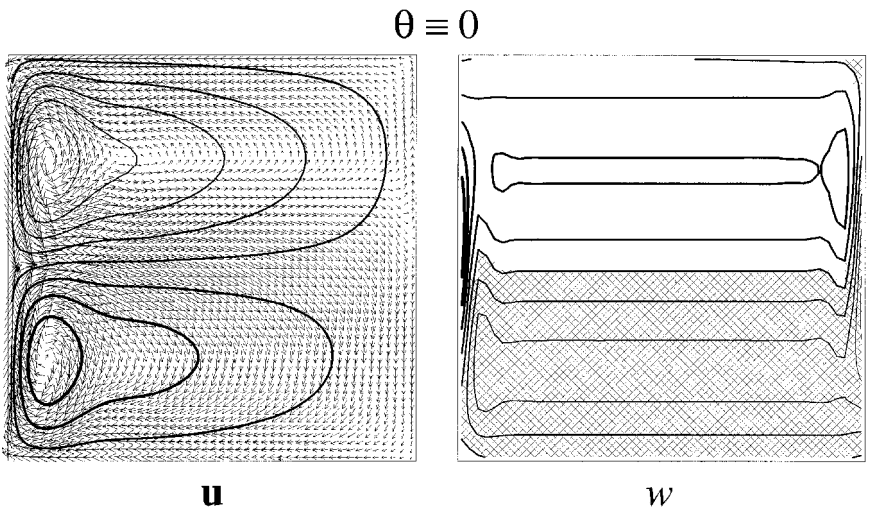

Figure 2. Solution of the lattice Boltzmann model with uniform buoyancy and the two-gyre wind stress (6.2). Left: The horizontal velocity (arrows) and the dynamic height (contours, with darker lines corresponding to larger dynamic height) at 160 m depth, just below the wind forcing layer. The maximum velocity is 3.78 km day^{-1}, and the rms velocity is 0.74 km day^{-1}. The range in dynamic height is 13.62 cm. To reduce the contrast in arrow sizes, the arrows are proportional to the *square root* of the fluid speed. Right: The vertical velocity at the same depth. The maximum (minimum) vertical velocity of 1.73×10^{-4} (-1.53×10^{-4}) km day^{-1} occurs at the western (eastern) boundary. The downwelling regions are hatched.

boundary conditions required larger values of viscosity to resolve the Ekman layers. However, because of the linkage $A_v = \delta^2 A_h$ between vertical and horizontal diffusivities, those more viscous solutions had unrealistically wide western boundary layers.[7]

For reference, we first examine the steady final state of a homogeneous ($\theta \equiv 0$) ocean with the wind forcing (6.1). The horizontal flow is geostrophic and z-independent below the wind forcing layer near the surface. This surface forcing layer plays the same role as the classical Ekman layer, creating a horizontal divergence that drives the deep interior by vortex stretching associated with depth-independent $\partial w/\partial z$. Figure 2 shows a plan view of pressure, horizontal velocity, and vertical velocity at a depth just below the surface forcing layer. The horizontal velocity in Figure 2 corresponds closely to Munk's classic model with no-slip conditions; the no-stress boundary conditions cause only a slight change in the structure of the western boundary layer. The western boundary layer is the only boundary layer present at leading order, because the Sverdrup and Ekman transport velocities have

7. The linkage between horizontal and vertical diffusivities results from the use of a single relaxation coefficient λ in the lattice Boltzmann equation for the mass particles. To obtain independent viscosities, one must generalize the method by (roughly speaking) relaxing horizontally moving particles toward the average of the horizontal particles at a different rate from the corresponding vertical relaxation. However, in this initial application to three-dimensional flow, I thought it best to take the simpler alternative of "isotropic diffusivity in scaled coordinates."

no components normal to the northern, southern and eastern boundaries. The upwelling (downwelling) observed at the western (eastern) boundaries is a response to the *second order* interior flow. At second order in the viscosity, the interior velocity acquires an eastward, downwind component; this requires downwelling near the surface at the eastern boundary and upwelling near the western boundary to maintain mass balance. However, these up- and downwelling velocities are the same size as the interior vertical velocity—not $E_h^{-1/3}$ larger, as would be expected in *leading order* sidewall upwelling layers. In the stratified solutions to be described next, the interior velocity acquires a (leading order) thermal wind component normal to the coastline; mass balance then requires upwelling boundary layers with vertical velocities much larger than the interior vertical velocity.

Solutions with nonuniform buoyancy require sources and sinks of buoyancy to maintain a realistic buoyancy range in the face of diffusion. In reality, all of these sources and sinks lie near the ocean surface. However, ocean surface cooling tends to produce regions of static instability, which usually require an externally imposed *convective adjustment* to restore neutral stability. The convective adjustment is distasteful because it is completely arbitrary, and because it can become a source of computational noise; see Cessi (1996) and Cessi and Young (1996).

In both primitive equation models and planetary geostrophic models, static instability occurs because the typically very small aspect ratio of the gridboxes inhibits convection. Linear stability theory predicts that the fastest growing convective cells have horizontal and vertical scales comparable to, or somewhat smaller than, the ocean depth. Thus models with horizontal grid spacing much larger than the ocean depth do not resolve the fastest growing cells. On the other hand, because the LB model effectively imposes unit aspect ratio in scaled variables, the most unstable convective cells have a real (dimensional) horizontal scale about 1000 times larger than the vertical scale. Thus the LB model resolves convection, but the convection occurs at an unrealistically large horizontal scale. Convective adjustment may still be required, but it seems to play a less essential role than in the more conventional models.

We examine 3 solutions with non-uniform stratification. The first solution (solution A) has no convective adjustment, but the diabatic heating is especially chosen to avoid static instability. Solution A is steady; its regions of static instability are very small; and spontaneous convection seems to be absent. The second solution (solution B) also lacks convective adjustment, but the diabatic forcing includes a significant surface cooling at high latitude. Solution B is unsteady, with persistent large-scale spontaneous convection occurring near the northern boundary. The third solution (solution C) has the same diabatic heating as B but also includes an arbitrary convective adjustment. The convective adjustment in C removes most of the unsteady convection present in B, but the two solutions are otherwise surprisingly similar.

All three solutions, A, B and C, have the geometry, dissipation parameters, and wind forcing described above. They differ only in the presence or absence of convective adjustment, in the diabatic heating term $Q(x, y, z)$ on the right-hand side of the buoyancy

equation (5.8d), and in the boundary condition on θ at the ocean bottom. In solution A, we take

$$Q = e^{z/d} \cos\left(\frac{\pi y}{2L}\right)(\theta^* - \theta_{sfc})/\tau, \qquad 0 < y < L, \tag{6.3}$$

where d is the same as in (6.1), θ^* and τ are prescribed constants, and $\theta_{sfc}(t)$ is the average buoyancy at the ocean surface. We take $\theta = 0$ as the boundary condition on buoyancy at the ocean bottom. At all other boundaries, the boundary conditions are no normal flux of θ, corresponding to elastic collisions of the buoyancy particles with the boundary in the LB model. Thus, in solution A, we heat the ocean surface layer everywhere, but more intensely in the south, until the difference between the average surface buoyancy θ_{sfc} and the uniform bottom buoyancy approaches the prescribed value θ^*; τ is the time-scale for the adjustment. We regard the uniform bottom buoyancy as resulting from the sinking and subsequent spreading of cold water near the northern boundary by small-scale processes not contained in the model. Alternatively, we could regard solution A as a model of, say, the upper half ocean, with the bottom boundary condition corresponding to a uniformly cold abyss.

In solution B, we take

$$Q = e^{z/d}\left(\theta^* \cos\left(\frac{\pi y}{2L}\right) - \theta\right)\Big/ \tau, \tag{6.4}$$

where θ^* and τ are constants with the same values as in solution A, and we take the lower boundary condition to be no flux of θ into the ocean bottom. In (6.4) θ is the local value of buoyancy; thus (6.4) corresponds to "surface restoring conditions" of the kind often used in ocean circulation models. At equilibrium, the average volume integral of (6.4) vanishes. Hence the diabatic forcing (6.4) corresponds to heating near the ocean surface in the southern ocean and surface cooling in the north. The surface cooling produces a large region of static instability. Nevertheless, we do not apply convective adjustment to solution B.

In solution C, we take the same diabatic forcing (6.4) and bottom boundary condition as in solution B, but we apply a convective adjustment in the form of an additional term,

$$Q_c = (\theta_{sort} - \theta)/\tau_c, \tag{6.5}$$

on the right-hand side of the buoyancy equation. Here, θ_{sort} is the buoyancy corresponding to a vertical sorting (to produce buoyancy increasing upward) of the buoyancy at each horizontal location, and τ_c is the time scale for convective adjustment. Thus Q_c vanishes if the water column is statically stable. In all three solutions, A, B and C, we take $\tau = 1$ year and θ^* to be the change in buoyancy corresponding to 2 units of σ_θ. In solution C, we take $\tau_c = 5$ days.

We begin our discussion of the 3 stratified solutions with a brief overall summary. The greatest differences are between solutions A and B. In solution A, with surface heating (6.3)

and bottom boundary condition $\theta = 0$, the surface buoyancy range of 0.66 sigma units (sgu) is much smaller than the imposed difference of 2.0 sgu between the average surface buoyancy and the uniform buoyancy at the ocean bottom. The net heat flux is downward and through the ocean bottom. The flow is statically stable except within a few small and extremely thin surface regions in which cold water flows southward over warmer water. Unsurprisingly therefore, solution A resembles the predictions of the linear theory of wind-driven ocean circulation, in which the mean buoyancy varies only with depth.

In solution B, with surface heating in the south, cooling in the north, and no buoyancy flux through the bottom, the net heat flux is northward. The surface buoyancy range of 1.67 sgu is comparable to the average difference between the surface and bottom, and the flow contains a strong thermohaline component. Solution B is statically unstable in a relatively deep layer covering the northeastern third of the ocean basin. This layer of static instability reaches depths greater than 1 km along the northern boundary. Within and below this unstable layer, we observe unsteady convective motions with horizontal scales of hundreds of kilometers. Time-averaging smooths out these convective eddies but has little other effect on the solution; hence we prefer to view "snapshots" of solution B.

Solution A begins in a state of rest with $\theta \equiv 0$. After 235 years it seems to have reached a steady state. All the pictures of A correspond to this time. Solution B begins at the end-state of A. All the pictures of B correspond to a time 86 years later, by which B has achieved a statistically steady state. Solution C begins from B, and spans an additional 25 years. At 50^3 resolution, the solutions require 1.23 sec per time step, that is, 91.4 minutes per simulated year, on a desktop workstation with a 170 Mhz processor.

Figure 3 shows the horizontal velocity and dynamic height (top), buoyancy (middle), and vertical velocity (bottom) at a level just below the surface forcing layer in solutions A (left) and B (right). Figure 4 shows the corresponding quantities at mid-depth. Figures 5 and 6 show sections of buoyancy. Since the ocean bottom is flat, all of our solutions have the same, steady, depth-averaged flow. Once again, this depth-averaged flow is just the Munk solution for the wind (6.2) and is very similar to the sub-surface-layer flow shown in Figure 2 for the homogeneous solution. The near-surface flow in A (Fig. 3, upper left) closely resembles the Munk solution. The sub-thermocline flow (Fig. 4, upper left) is much weaker, except in the western subpolar gyre, where relatively cold water outcrops at the sea surface, and the wind-driven circulation penetrates deepest. The near-surface vertical velocity (Fig. 3, bottom left) resembles the homogeneous case (Fig. 2, right) in the interior ocean, but shows a region of very strong upwelling along the western boundary. This upwelling region, which extends through the full depth of the thermocline (about 1 km maximum at the western boundary), occurs where the interior thermal wind has a strong offshore component. The upwelling along the western boundary feeds this offshore flow and bends the isopycnals upward near the boundary (Fig. 6).

In solution B, the diabatic heating produces a strong surface buoyancy gradient (Fig. 3, middle right) with virtually no closed contours of buoyancy. The corresponding thermal wind dominates the surface flow in the subpolar gyre (Fig. 3, upper right) so that the flow is

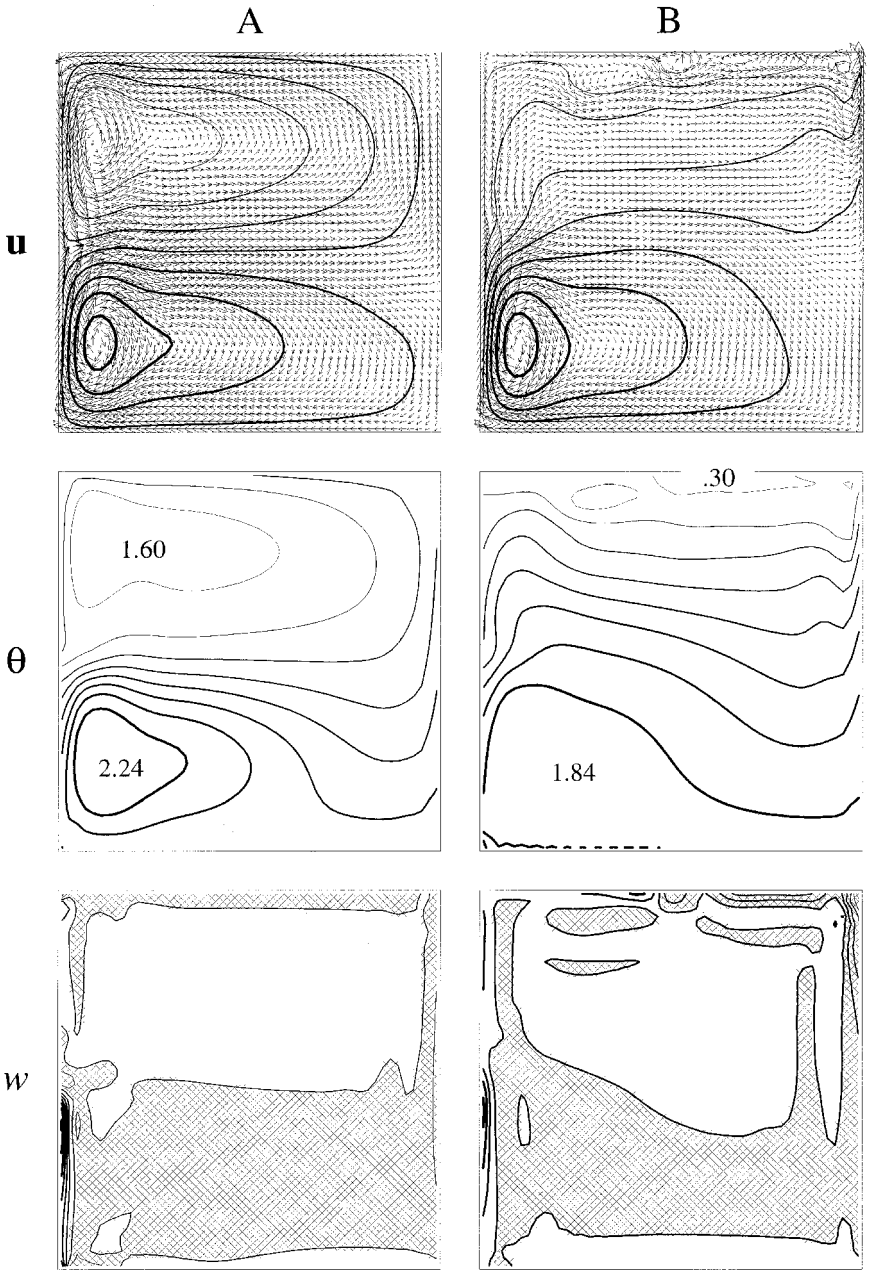

Figure 3. The horizontal velocity and dynamic height (top), buoyancy (middle), and vertical velocity (bottom) at a level just below the wind forcing layer in solution A (left) and B (right). Arrows are proportional to the square root of the velocity, and darker contours correspond to larger values. The maximum (and rms) horizontal velocities are 19.22 (3.32) km day^{-1} in solution A and 40.22 (5.64) km day^{-1} in B. The buoyancy extrema (middle) are in units of σ_θ. The vertical velocity ranges between -9.39×10^{-4} and 1.95×10^{-3} km day^{-1} in A (lower left), and between -9.66×10^{-3} and 5.34×10^{-3} km day^{-1} in B (lower right). Downwelling regions are hatched.

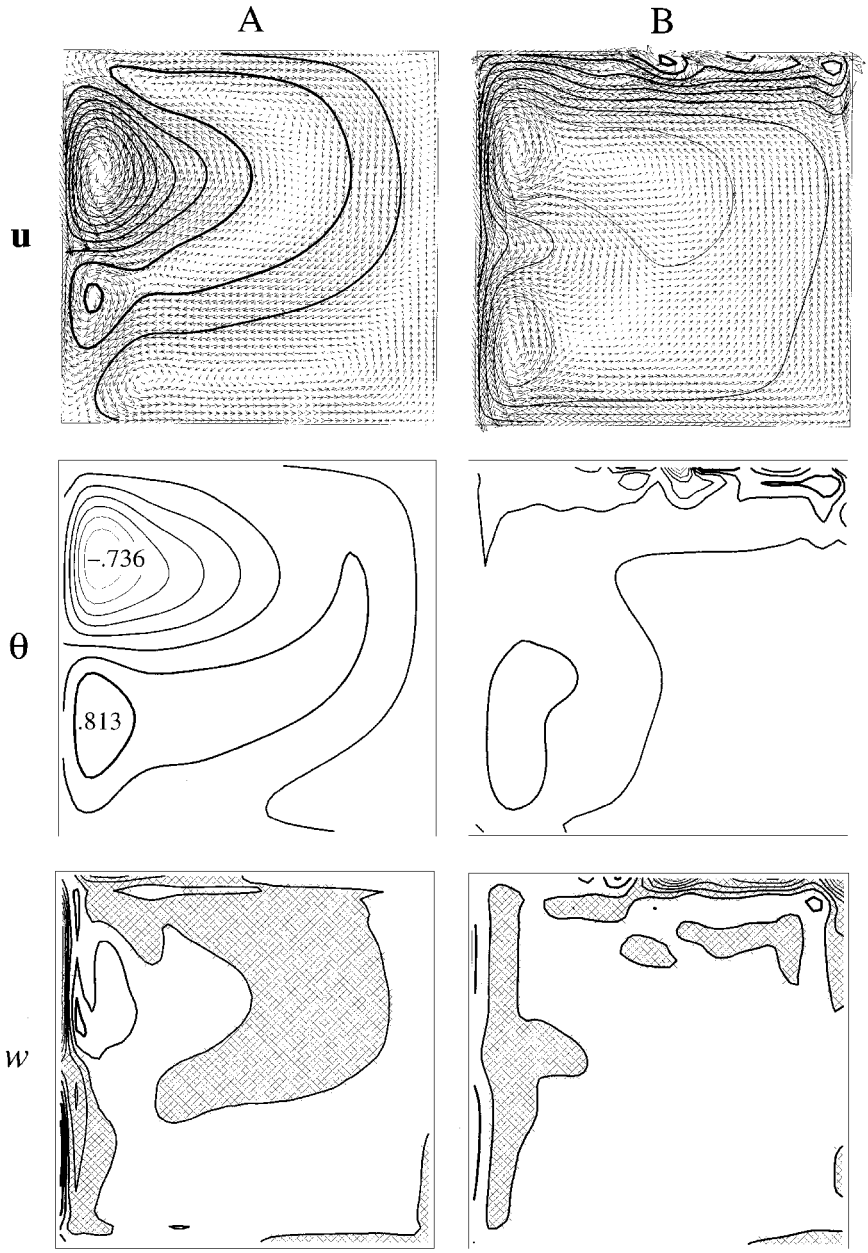

Figure 4. The same as Figure 3, but in mid-water, at a depth of 2 km. The maximum horizontal velocity in solution A (1.50 km day^{-1}, top left) arises from the deep penetration of the subpolar wind gyre. In B, sinking along the northern boundary feeds a southward-flowing deep western boundary current (top right) with a maximum velocity of 6.09 km day^{-1}. The buoyancy range in B (1.82 sigma units, middle right) is more than twice as great as in A (middle left, 0.77 sgu) and is clearly associated with the convection. Because of convection, the vertical velocity is more than an order of magnitude larger in B (lower right, range -8.83×10^{-3} to $+2.74 \times 10^{-3}$ km day^{-1}) than in A (lower left, range -1.77×10^{-4} to $+1.16 \times 10^{-4}$ km day^{-1}).

eastward throughout most of the interior ocean. The strongest upwelling occurs at the subtropical western boundary (as in A) but the strongest downwelling occurs in the northeastern region of unsteady convection, where the the horizontal flow converges (Fig. 3, lower right). Below the thermocline, solution B differs strikingly from A. The sinking along the northern boundary penetrates the deep ocean (Figure 4, lower right), driving a westward flowing northern boundary layer and a southward flowing deep western boundary current (Fig. 4, upper right). Because the transport in the deep western boundary current exceeds the Sverdrup transport in the subpolar gyre, the surface flow is actually northward in the subpolar western boundary layer (Figure 3, upper right). The downwelling along the northern boundary in B is balanced by a deep upwelling (and corresponding poleward flow) that, in contrast to A, covers nearly the whole interior ocean (Fig. 4, lower right). This deep upwelling produces a much sharper internal boundary layer in B than in A; see Figures 5 and 6. In overall summary, the thermohaline circulation appears to be unrealistically strong in solution B and unrealistically weak in A, but the two solutions show many of the features anticipated by the classical theories of ocean circulation.

In solution C, the addition of the convective adjustment (6.5) with an adjustment time $\tau_c = 5$ days removes most of the *unsteady* convective motions but has relatively little other effect on the flow. In fact, pictures of solution C closely resemble time-averages of B. Figure 7 shows the minimum and maximum Vaisala frequency N at each horizontal location in solutions B and C. Figure 8 shows a section of N from south to north along $x = 2L/3$. We take N as positive if $N^2 > 0$, and we define N to be a negative real number if $N^2 < 0$. Thus the hatched regions in Figures 7 and 8 correspond to regions of static instability. We see that the convective adjustment reduces the amplitude and extent of static instability, but produces significant noise on the scale of the lattice. When the time scale τ_c for convective adjustment was reduced from 5 days to 1 day (to make the adjustment almost instantaneous), this noise reached an unacceptable level. From Figures 5B and 5C we see that the region of active convection in B becomes a region of nearly vertical isobuoyancy lines in C. However, this seems to be the only significant difference between C and time averages of B. Thus convective adjustment seems both harmful and unnecessary when the model can resolve its own convection.

The LB model differs from conventional primitive equation models in that it does not *impose* hydrostatic balance. We test for hydrostatic balance by computing the quantity

$$\mu \equiv \frac{H}{f_0 UL} |\phi_z - \theta|, \tag{6.6}$$

where $U = 1$ km day^{-1} is the scale for horizontal velocity. If the flow is hydrostatic, $\mu \ll 1$. In the homogeneous solution depicted in Figure 2, the field of μ at mid-depth has a maximum of 2.5×10^{-3}, thus, as expected, the homogeneous solution is hydrostatic. In solution A, the stratified solution heated from above and cooled from below, the mid-depth μ shows a maximum of only 0.023; solution A is also hydrostatic. Solutions B and C, with

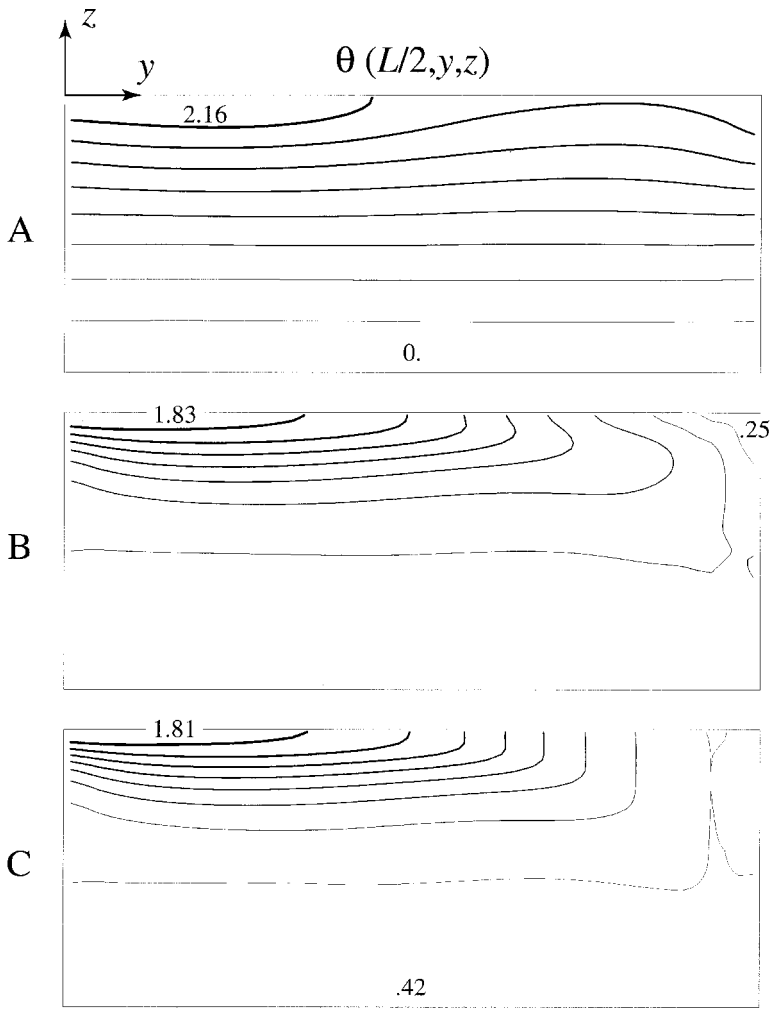

Figure 5. South-north sections of buoyancy at mid-basin, $x = L/2$, in solutions A, B and C. The maximum and minimum values are given in sigma units. The convective adjustment in C causes the iso-buoyancy lines to become vertical in regions where solution B is statically unstable but produces little other effect.

surface cooling, showed significant departures from hydrostatic balance but only in a narrow region near the northern boundary, where μ attained respective maxima of 1.01 and 0.28. In summary then, the solutions of the LB model are hydrostatic almost everywhere, despite the artificial enhancement of inertia and friction in the vertical momentum equation. Significant departures from hydrostatic balance occur only in the regions of strong static instability.

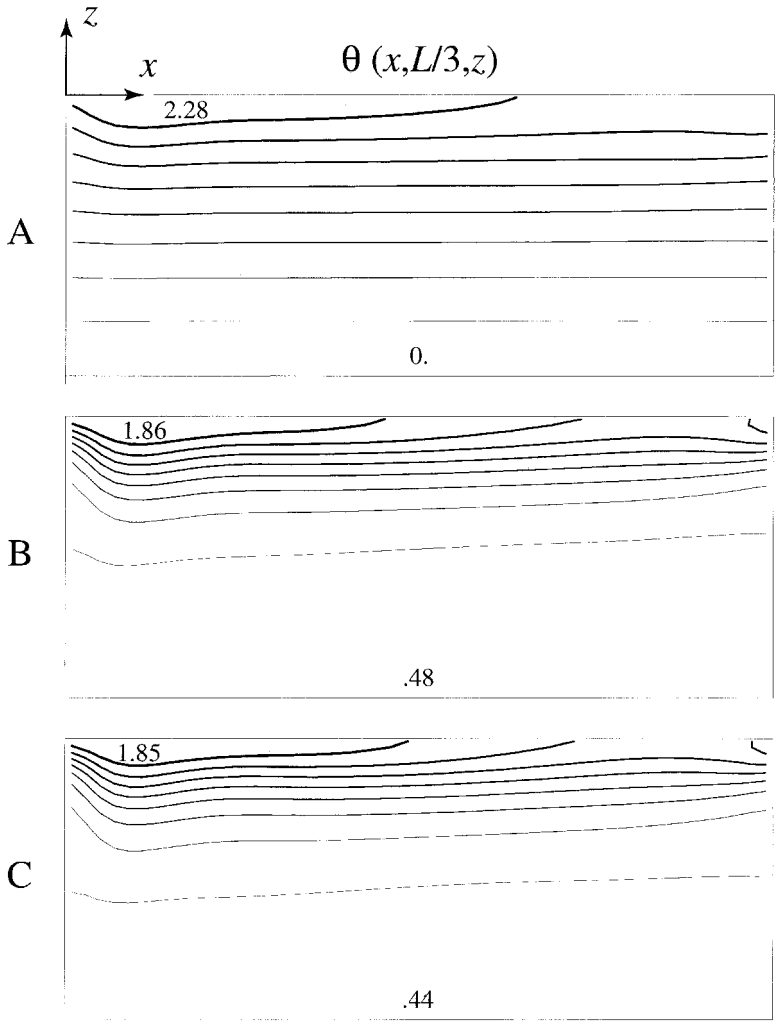

Figure 6. East-west sections of buoyancy (sigma units) in the subtropical gyre at $y = L/3$, in solutions A, B, and C. The deep upwelling required to balance the sinking of cold water near the northern boundary produces a much sharper thermocline in B and C, but the convective adjustment present in C has little effect on the subtropical gyre.

7. Discussion

The most attractive feature of the lattice Boltzmann method is its stark simplicity. The 6 steps of the LB algorithm, summarized in (5.1–7), are easy to code and easy to check for errors. Even more significantly—although I have not taken advantage of this yet—these steps are massively parallel. The parallelism reflects the philosophy of LB that all the physics is local. Nevertheless, it is easy to foresee that numerical ocean circulation models will eventually blend LB methodology with more conventional methods based on finite

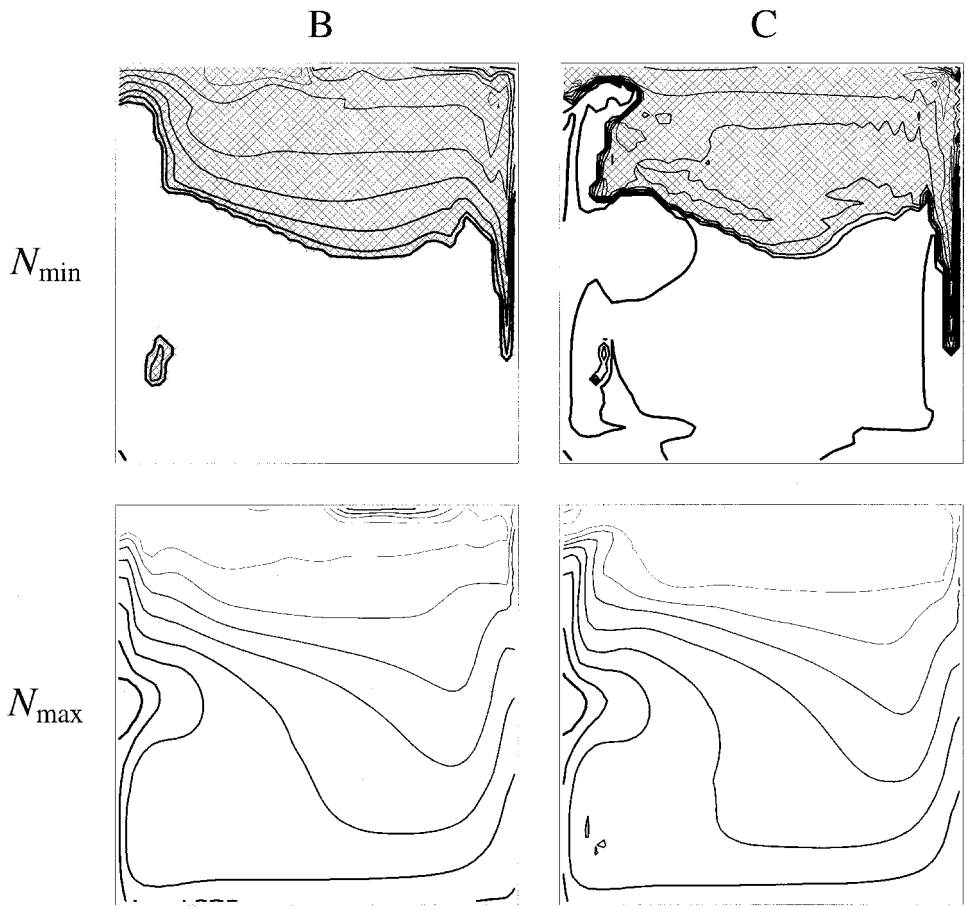

Figure 7. The minimum (top) and maximum (bottom) Vaisala frequency N in the water column in solutions B (left) and C (right). These two solutions differ only in the presence of the convective adjustment in C. In B, the minimum N (top left) varies between -2.25 and $+.365$ cycles per hour (cph) with negative values (corresponding to hatched regions on the figure) denoting static instability. Convective adjustment reduces static instability—the minimum N varies between $-.543$ and $+.361$ cph in solution C (upper left)—but introduces a significant noise on the lattice scale. The maximum N in the water column is very similar in the two solutions. Its range in B (lower left) is $+.487$ to $+2.84$ cph; its range in C (lower right) is $+.486$ to $+2.96$ cph.

differences, combining the stability and efficiency of the former with the greater flexibility of the latter.

The present application adheres almost completely to the LB philosophy that the interactions between particles be purely local. A strict adherence to this philosophy seemed appropriate in this initial application of the method to 3-dimensional ocean circulation, and it led almost inevitably to the enhancement of inertia and friction in the vertical momentum equation associated with small aspect ratio. The effects of this enhancement, especially the

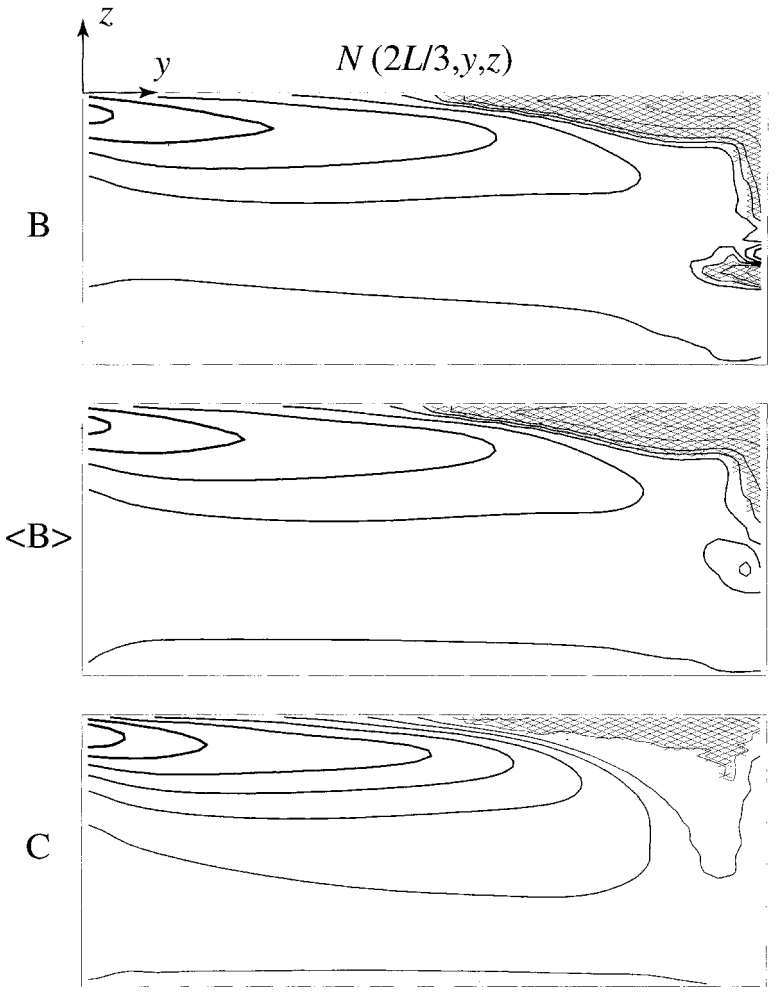

Figure 8. The Vaisala frequency N in a south-north section at $x = 2L/3$ in a snapshot of solution B (top, range −.448 to +.652 cycles per hour), the time-average of B over 37 years (middle, −.451 to +.643 cph), and in solution C (bottom, −.105 to +.666 cph). Negative values, denoting static instability, correspond to hatched regions on the figure.

ability to resolve upwelling boundary layers and unsteady convection, seem wholly beneficial. This is a strategy that could, and perhaps should, be applied to more conventional models. However, it is possible, even within the philosophy of LB, to adopt a completely different strategy, and regard all the particles in a vertical column as "internal variables" at the same location. In this approach, the physics of the vertical momentum equation is contained within the rules for the collisions between particles at the same horizontal location, and hydrostatic balance could even be regarded as a "conservation law" to be respected by the collisions. The collisions would thus represent a kind of

"meta" convective adjustment, whose precise form would undoubtedly require much investigation.

S99 offered 2 conjectures which must now be retracted. The first was that a 7-velocity model, the 3-dimensional analogue of the 4-velocity model described in Section 5 of S99, would prove adequate for solutions of the 3-dimensional planetary geostrophic equations despite the peculiar, anisotropic friction of the 7-velocity model. Unfortunately, solutions of the 7-velocity model were found to contain spurious oscillations which could, in hindsight, be attributed to the form of the friction. S99 also conjectured that a 27-velocity model would be required to simulate Navier-Stokes viscosity in 3 dimensions. However, solutions of the 27-velocity model were found to be virtually identical to solutions of the 15-velocity model described in this paper.

The incorporation of realistic bathymetry is the biggest remaining challenge in the development of an LB ocean circulation model. Although the LB method may be extended to wholly irregular lattices, it loses much of its appeal, and computer storage requirements quickly become prohibitive. The better strategy is to retain the regular lattice, and to incorporate realistic bathymetry into the rules governing particle collisions with the ocean bottom. Since the lattice points along the ocean bottom constitute a "subset of zero measure" of the set of all lattice points, the relatively complicated collision rules required to simulate arbitrary bottom topography do not harm the efficiency of the LB method. Preliminary experiments with smooth bottom topography give excellent results.

Acknowledgments. This work was supported by the National Science Foundation, grant OCE-9521004. I thank George Veronis for his comments, Breck Betts for his help with the figures, and Larisa Salmon for her construction of a cardboard model.

APPENDIX A

Derivation of the viscosity

To consistent order, we may solve the first order approximation, $\Gamma^{(0)}_{nmk} = 0$, to (2.21) for

$$D_{nmk}\rho^{eq}_{nmk} = -\rho^{(1)}_{nmk} \tag{A.1}$$

and use (A.1) to eliminate ρ^{eq}_{nmk} from the second order expression (2.23), which then becomes

$$\Gamma^{(1)}_{nmk} = -\frac{\Delta t}{2} D_{nmk}\rho^{(1)}_{nmk} + \varepsilon D_{nmk}\rho^{(1)}_{nmk} + \varepsilon\rho^{(2)}_{nmk}. \tag{A.2}$$

The conservation relations (2.24) imply (2.30) and

$$\sum_{nmk} c_{nmk,\alpha}\Gamma^{(1)}_{nmk} = \left(\varepsilon - \frac{\Delta t}{2}\right)\sum_{nmk} c_{nmk,\alpha}D_{nmk}\rho^{(1)}_{nmk} = \left(\varepsilon - \frac{\Delta t}{2}\right)\frac{\partial}{\partial x_\beta}\sum_{nmk} c_{nmk,\alpha}c_{nmk,\beta}\rho^{(1)}_{nmk}. \tag{A.3}$$

Repeated Greek subscripts are summed from 1 to 3. To consistent order, we may use (A.1) again to express (A.3) solely in terms of the equilibrium densities. Thus

$$\begin{aligned}
&\sum_{nmk} c_{nmk,\alpha}\Gamma^{(1)}_{nmk} \\
&\quad = -\left(\varepsilon - \frac{\Delta t}{2}\right)\frac{\partial}{\partial x_\beta}\sum_{nmk} c_{nmk,\alpha}c_{nmk,\beta}D_{nmk}\rho^{eq}_{nmk} \\
&\quad = -\left(\varepsilon - \frac{\Delta t}{2}\right)\frac{\partial}{\partial x_\beta}\left(\frac{\partial}{\partial t}\sum_{nmk} c_{nmk,\alpha}c_{nmk,\beta}\rho^{eq}_{nmk} + \frac{\partial}{\partial x_\gamma}\sum_{nmk} c_{nmk,\alpha}c_{nmk,\beta}c_{nmk,\gamma}\rho^{eq}_{nmk}\right) \\
&\quad = -\left(\varepsilon - \frac{\Delta t}{2}\right)\left(\frac{\partial}{\partial x_\beta}\frac{\partial}{\partial t}P_{\alpha\beta} + \frac{\partial}{\partial x_\beta}\frac{\partial}{\partial x_\gamma}\sum_{nmk} c_{nmk,\alpha}c_{nmk,\beta}c_{nmk,\gamma}B_{nmk}\left(n\frac{u}{c_h} + m\frac{v}{c_h} + k\frac{w}{c_v}\right)\right)
\end{aligned} \tag{A.4}$$

where we have used (2.20), (2.26) and (2.10). Suppose $\alpha = 1$. Then, using (2.17) and (2.27a), (A.4) becomes

$$\begin{aligned}
\sum_{nmk} c_{nmk,1}\Gamma^{(1)}_{nmk} = -\left(\varepsilon - \frac{\Delta t}{2}\right)\Bigg\{&-\frac{c_h^2}{3}\frac{\partial}{\partial x}\nabla\cdot\mathbf{v} + \frac{1}{c_h^2}\frac{\partial^2 u}{\partial x_\beta \partial x_\gamma}\sum_{nmk} c_{nmk,1}c_{nmk,\beta}c_{nmk,\gamma}c_{nmk,1}B_{nmk} \\
&+ \frac{1}{c_h^2}\frac{\partial^2 v}{\partial x_\beta \partial x_\gamma}\sum_{nmk} c_{nmk,1}c_{nmk,\beta}c_{nmk,\gamma}c_{nmk,2}B_{nmk} \\
&+ \frac{1}{c_v^2}\frac{\partial^2 w}{\partial x_\beta \partial x_\gamma}\sum_{nmk} c_{nmk,1}c_{nmk,\beta}c_{nmk,\gamma}c_{nmk,3}B_{nmk}\Bigg\}.
\end{aligned} \tag{A.5}$$

Using (2.4) and (2.11–13), we find that

$$\frac{1}{c_h^2}\frac{\partial^2 u}{\partial x_\beta \partial x_\gamma}\sum_{nmk} c_{nmk,1}c_{nmk,\beta}c_{nmk,\gamma}c_{nmk,1}B_{nmk} = c_h^2 u_{xx} + \frac{1}{3}c_h^2 u_{yy} + \frac{1}{3}c_v^2 u_{zz}. \tag{A.6}$$

Similarly,

$$\frac{1}{c_h^2}\frac{\partial^2 v}{\partial x_\beta \partial x_\gamma}\sum_{nmk} c_{nmk,1}c_{nmk,\beta}c_{nmk,\gamma}c_{nmk,2}B_{nmk} = \frac{2}{3}c_h^2 v_{xy} \tag{A.7}$$

and

$$\frac{1}{c_v^2}\frac{\partial^2 w}{\partial x_\beta \partial x_\gamma}\sum_{nmk} c_{nmk,1}c_{nmk,\beta}c_{nmk,\gamma}c_{nmk,3}B_{nmk} = \frac{2}{3}c_h^2 w_{xz}. \tag{A.8}$$

Substituting (A.6–8) into (A.5), we obtain

$$\sum_{nmk} c_{nmk,1}\Gamma^{(1)}_{nmk} = -\left(\varepsilon - \frac{\Delta t}{2}\right)\frac{1}{3}(c_h^2 u_{xx} + c_h^2 u_{yy} + c_v^2 u_{zz} + c_h^2(\nabla_3\cdot\mathbf{v})_x). \tag{A.9}$$

Proceeding in a similar manner, we find that

$$\sum_{nmk} c_{nmk,2}\Gamma^{(1)}_{nmk} = -\left(\varepsilon - \frac{\Delta t}{2}\right)\frac{1}{3}\left(c_h^2 v_{xx} + c_h^2 v_{yy} + c_v^2 v_{zz} + c_h^2(\nabla_3 \cdot \mathbf{v})_y\right) \tag{A.10}$$

and

$$\sum_{nmk} c_{nmk,3}\Gamma^{(1)}_{nmk} = -\left(\varepsilon - \frac{\Delta t}{2}\right)\frac{1}{3}\left(c_h^2 w_{xx} + c_h^2 w_{yy} + c_v^2 w_{zz} + c_v^2(\nabla_3 \cdot \mathbf{v})_z\right). \tag{A.11}$$

In many applications of Navier-Stokes theory, the $\nabla_3 \cdot \mathbf{v}$ term is negligible. However, the *transient* LB dynamics has significant compressibility. Substituting $\rho_t = -\nabla_3 \cdot \mathbf{v}$ into (A.9–11), we obtain (2.31).

APPENDIX B

Derivation of the buoyancy equation

We derive (3.8) in a manner very similar to the derivation of (2.32). Expanding (3.3) in Δt, and substituting

$$\theta_i = \theta_i^{eq} + \varepsilon\theta_i^{(1)} + \varepsilon^2\theta_i^{(2)} + \cdots \tag{B.1}$$

where now $\varepsilon = \Lambda^{-1}$, we obtain

$$\gamma_i^{(0)} + \gamma_i^{(1)} + \cdots = 0, \tag{B.2}$$

where

$$\gamma_i^{(0)} \equiv D_i\theta_i^{eq} + \theta_i^{(1)} \tag{B.3}$$

contains all the first order terms, and

$$\gamma_i^{(1)} \equiv \frac{\Delta t}{2} D_i^2\theta_i^{eq} + \varepsilon D_i\theta_i^{(1)} + \varepsilon\theta_i^{(2)} \tag{B.4}$$

contains all the terms of order Δt or ε. Here,

$$D_i \equiv \frac{\partial}{\partial t} + c_{i\alpha}\frac{\partial}{\partial x_\alpha} \tag{B.5}$$

is the advection operator in the direction of the i-th particle, with $c_{i\alpha} = \mathbf{c}_i \cdot \mathbf{e}_\alpha$, and repeated Greek subscripts are summed from 1 to 3. We obtain the evolution equation for θ by applying Σ_i to (B.2). Since (B.1) and (3.5) imply

$$\sum_i \theta_i^{(1)} = \sum_i \theta_i^{(2)} = 0, \tag{B.6}$$

we obtain

$$\sum_i \gamma_i^{(0)} = \frac{\partial \theta}{\partial t} + \nabla \cdot (\theta \mathbf{v}). \tag{B.7}$$

Since (B.2–3) implies

$$D_i \theta_i^{eq} = -\theta_i^{(1)} \tag{B.8}$$

at leading order, we have the consistent order approximation

$$\gamma_i^{(1)} = \left(\varepsilon - \frac{\Delta t}{2}\right) D_i \theta_i^{(1)} + \varepsilon \theta_i^{(2)}. \tag{B.9}$$

Hence, using (B.6),

$$\sum_i \gamma_i^{(1)} = \left(\varepsilon - \frac{\Delta t}{2}\right) \sum_i D_i \theta_i^{(1)} = \left(\varepsilon - \frac{\Delta t}{2}\right) \frac{\partial}{\partial x_\alpha} \sum_i c_{i\alpha} \theta_i^{(1)}. \tag{B.10}$$

Using (B.8) again and (3.6), this becomes

$$\begin{aligned} \sum_i \gamma_i^{(1)} &= -\left(\varepsilon - \frac{\Delta t}{2}\right) \frac{\partial}{\partial x_\alpha} \sum_i c_{i\alpha} D_i \theta_i^{eq} \\ &= -\left(\varepsilon - \frac{\Delta t}{2}\right) \frac{\partial}{\partial x_\alpha} \left(\frac{\partial}{\partial t} (\theta v_\alpha) + \frac{\partial}{\partial x_\beta} \sum_i c_{i\alpha} c_{i\beta} \theta_i^{eq} \right) \\ &= -\left(\varepsilon - \frac{\Delta t}{2}\right) \left\{ \nabla_3 \cdot \frac{\partial}{\partial t} (\theta \mathbf{v}) + \frac{c_h^2}{3} \left(\frac{\partial^2 \theta}{\partial x^2} + \frac{\partial^2 \theta}{\partial y^2} \right) + \frac{c_v^2}{3} \frac{\partial^2 \theta}{\partial z^2} \right\}. \end{aligned} \tag{B.11}$$

Thus by (B.7) and (B.11), the i-summation of (B.2) is equivalent to (3.8).

APPENDIX C

Higher order terms arising from buoyancy force

Since the generalization (3.11) of the equilibrium densities satisfies (2.14–15), (2.24) still apply. Hence (2.22) and the horizontal components of (2.26) are unchanged. The vertical component of (2.26) acquires the term $-\delta^2 \theta$. At the next order, (2.30) still holds but (2.31) does not; in the last line of (A.4), the term

$$\frac{\partial^2 P_{33}}{\partial z \partial t} = \delta^2 \frac{\partial}{\partial t} (\phi_z - \theta) \tag{C.1}$$

by (3.12–13). The latter term contributes the θ_t-term to (3.14).

APPENDIX D

Proof that (4.14) corresponds to Coriolis force

We expand (4.14) in Δt, keeping terms of first and second order. Remembering that $A_{\alpha\beta} = O(\Delta t)$, we have, to consistent order,

$$\begin{aligned}
&\left(\Delta t D_{nmk} + \frac{1}{2}(\Delta t)^2 D_{nmk}^2\right)\rho_{nmk} \\
&\quad = \frac{B_{nmk}}{c_h^2} c_{nmk,\alpha} A_{\alpha\beta} \sum_{rsp} c_{rsp,\beta}\rho_{rsp} + \frac{B_{nmk}}{c_h^2} c_{nmk,\alpha} A_{\alpha\beta} \sum_{rsp} c_{rsp,\beta} \\
&\qquad \cdot \left\{\rho_{rsp} + \Delta t(\mathbf{c}_{nmk} - \mathbf{c}_{rsp})\cdot\nabla\rho_{rsp} + \frac{B_{rsp}}{c_h^2} c_{rsp,\gamma} A_{\gamma\delta} \sum_{abd} c_{abd,\delta}\rho_{abd}\right\} \\
&\qquad + \frac{B_{nmk}}{c_h^2} c_{nmk,\alpha}\Delta t(\mathbf{c}_{nmk}\cdot\nabla A_{\alpha\beta}) \sum_{rsp} c_{rsp,\beta}\rho_{rsp}
\end{aligned} \tag{D.1}$$

where all quantities are evaluated at $(\mathbf{x}, t)$ and repeated Greek indices are summed from 1 to 2 only (because $A_{\alpha\beta}$ has only horizontal components). That is,

$$\begin{aligned}
\left(\Delta t D_{nmk} + \frac{1}{2}(\Delta t)^2 D_{nmk}^2\right)\rho_{nmk} &= \frac{2B_{nmk}}{c_h^2} c_{nmk,\alpha} A_{\alpha\beta} u_\beta \\
&\quad + \frac{B_{nmk}}{c_h^2} c_{nmk,\alpha}\left\{\Delta t\left(\mathbf{c}_{nmk}\cdot\nabla(A_{\alpha\beta}u_\beta) - A_{\alpha\beta}\frac{\partial\phi}{\partial x_\beta}\right) + A_{\alpha\beta}A_{\beta\delta}u_\delta\right\}
\end{aligned} \tag{D.2}$$

where we have used (2.5–6), (2.28) and

$$\sum_{rsp} B_{rsp} c_{rsp,\beta} c_{rsp,\gamma} = c_h^2 \delta_{\beta\gamma}. \tag{D.3}$$

Substituting from (4.8), we obtain, to consistent order,

$$\begin{aligned}
&\left(\Delta t D_{nmk} + \frac{1}{2}(\Delta t)^2 D_{nmk}^2\right)\rho_{nmk} \\
&\quad = \frac{2B_{nmk}}{c_h^2} c_{nmk,\alpha}\left[\frac{f\Delta t}{2}\varepsilon_{\alpha\beta} - \frac{(f\Delta t)^2}{8}\delta_{\alpha\beta}\right] u_\beta + \frac{B_{nmk}}{c_h^2} c_{nmk,\alpha}\frac{(\Delta t)^2}{2} \\
&\qquad \cdot \left\{\varepsilon_{\alpha\beta}\left(\mathbf{c}_{nmk}\cdot\nabla(fu_\beta) - f\frac{\partial\phi}{\partial x_\beta}\right) + \frac{1}{2}f^2\varepsilon_{\alpha\beta}\varepsilon_{\beta\delta}u_\delta\right\}.
\end{aligned} \tag{D.4}$$

Using $\varepsilon_{\alpha\beta}\varepsilon_{\beta\delta} = -\delta_{\alpha\delta}$ and combining terms, this is

$$\left(\Delta t D_{nmk} + \frac{1}{2}(\Delta t)^2 D_{nmk}^2\right)\rho_{nmk} = \frac{2B_{nmk}}{c_h^2} c_{nmk,\alpha}\left[\frac{f\Delta t}{2}\varepsilon_{\alpha\beta} - \frac{(f\Delta t)^2}{4}\delta_{\alpha\beta}\right] u_\beta + \frac{B_{nmk}}{c_h^2}\frac{(\Delta t)^2}{2} c_{nmk,\alpha}\varepsilon_{\alpha\beta}\left(\mathbf{c}_{nmk}\cdot\nabla(fu_\beta) - f\frac{\partial\phi}{\partial x_\beta}\right). \tag{D.5}$$

The last line in (D.5) contributes at the second order. Thus we may consistently substitute the leading order momentum equation into the last term as follows:

$$\begin{aligned}\mathbf{c}_{nmk}\cdot\nabla(fu_\beta) - f\frac{\partial\phi}{\partial x_\beta} &= D_{nmk}(fu_\beta) - f\left(\frac{\partial u_\beta}{\partial t} + \frac{\partial\phi}{\partial x_\beta}\right)\\ &\approx D_{nmk}(fu_\beta) - f^2\varepsilon_{\beta\gamma}u_\gamma.\end{aligned} \tag{D.6}$$

Replacing the last parentheses in (D.5) by the final expression in (D.6) and cancelling some terms, we obtain an equation equivalent to (4.4) with $F_\alpha = f\varepsilon_{\alpha\beta}u_\beta$.

REFERENCES

Benzi, R., S. Succi and M. Vergassola. 1992. The lattice Boltzmann-equation—theory and applications. Phys. Rep., *222,* 145–197.

Cessi, P. 1996. Grid-scale instability of convective-adjustment schemes. J. Mar. Res., *54,* 407–420.

Cessi, P. and W. R. Young. 1996. Some unexpected consequences of the interaction between convective adjustment and horizontal diffusion. Physica D, *98,* 287–300.

Chen, S. and G. D. Doolen. 1998. Lattice Boltzmann method for fluid flows. Ann. Rev. Fluid Mech., *30,* 329–364.

Chen, S. Y., Z. Wang, X. W. Chan and G. D. Doolen. 1992. Lattice Boltzmann computational fluid dynamics in three dimensions. J. Stat. Phys., *68,* 379–400.

He, Xiaoyi and Li-Shi Luo. 1997. Theory of the lattice Boltzmann method: From the Boltzmann equation to the lattice Boltzmann equation. Phys. Rev. E, *56,* 6811–6817.

Huck, T., A. J. Weaver and A. Colin de Verdière. 1999. On the influence of the parameterization of lateral boundary layers on the thermohaline circulation in coarse-resolution ocean models. J. Mar. Res., *57,* 387–426.

Pedlosky, J. 1968. An overlooked aspect of the wind-driven ocean circulation. J. Fluid Mech., *32,* 809–821.

—— 1969. Linear theory of the circulation of a stratified ocean. J. Fluid Mech., *35,* 185–205.

Qian, Y. H., D. d'Humieres and P. Lallemand. 1992. Lattice BGK models for Navier-Stokes equation. Europhys. Lett., *17,* 479–484.

Rothman, D. H. and S. Zaleski. 1997. Lattice-Gas Cellular Automata: Simple Models of Complex Hydrodynamics, Cambridge, 297 pp.

Salmon, R. 1998. Lectures on Geophysical Fluid Dynamics, Oxford, 378 pp.

—— 1999. [S99] The lattice Boltzmann method as a basis for ocean circulation modeling. J. Mar. Res., *57,* 503–535.

Received: *25 October, 1999;* revised: *6 December, 1999.*